Instability of the Gulf Stream Front in the South Atlantic Bight

HUIJIE XUE* AND GEORGE MELLOR

Program in Atmospheric and Oceanic Sciences, Princeton University, Princeton, New Jersey

(Manuscript received 9 January 1992, in final form 8 December 1992)

ABSTRACT

To understand Gulf Stream meanders in the South Atlantic Bight, the growth of three-dimensional perturbations along two-dimensional frontal zones is examined by using linearized primitive equations. The Fourier–Galerkin method and the orthogonal collocation method are combined to formulate the spectral model. Emphasis is placed on the effects of cross-frontal topographic slope on the stability of the front, and on the characteristics of the most unstable modes. Attention is directed to the cross sections upstream and downstream of the Charleston Bump, which is a topographic feature near 31°N. The major results obtained from this linear study are that 1) the growth rate of the most unstable mode decreases and the associated phase speed increases after incorporating cross-front topographic gradients; 2) the most unstable solution found in the region downstream of the Charleston Bump has a slightly longer wavelength and slower phase speed than those found in the region upstream of the Bump.

1. Introduction

a. Observed meanders

Finite amplitude wavelike meanders are dominant mesoscale features of the Gulf Stream in the South Atlantic Bight (SAB) (Fig. 1). Webster (1961) described meanders off Onslow Bay as a type of skewed wave motion that consists of an intense offshore flow and a broad, confused onshore flow. In the 1970s and 1980s, several observational projects conducted in the SAB provide us with a considerable amount of information on meanders (Lee and Mayer 1979; Lee et al. 1981; Bane et al. 1981; Brooks and Bane 1983). A typical meander consists of a southwestward extrusion of warm Gulf Stream water, with cooler water entrained between the extrusion and the stream. The cyclonic circulation within the resulting cold water dome is consistent with upwelled isotherms, and the anticyclonic circulation within warm filaments is consistent with the downwelled isotherms. A warm filament reaches only a few tens of meters deep, while a cold water dome can reach a depth more than 200 m and extend shoreward beneath the warm filament. Meanders can develop into so-called "backward breaking" waves in two days. They occur on the average of once per week.

As meanders propagate northeastward in the SAB, their scales generally increase and their phase speeds decrease. Filaments off Georgia depicted by Lee et al. (1981) have offshore scales between 30 and 40 km and a depth of about 20 m. Their downstream scales range from 100 to 200 km. Embedded cold cores move downstream at speeds between 40 and 60 km day^{-1} (Lee and Atkinson 1983). Scales become larger in the region off South Carolina according to AXBT data analyzed by Bane et al. (1981). Warm filaments are about 50 km wide in the offshore direction and about 50 m deep. Downstream scales reach 200–300 km between Charleston and Cape Hatteras. A decrease in the phase speed between Charleston and Cape Hatteras was reported by both Legeckis (1979) and Bane et al. (1981). An average phase speed off Onslow Bay is approximately 35 km day^{-1} or less.

Many authors surmise that meanders result from local barotropic and baroclinic instabilities. The primary objective of carrying out instability studies is to find out how much of the observed phenomena can be explained by linear theory and to answer the following questions: 1) Is the Gulf Stream really unstable? 2) What is the role played by the bottom topography in producing meanders along the Gulf Stream front? 3) Are the changes of meander scales and propagation speeds due to changing characteristics of the most unstable wave associated with mean conditions at different cross sections?

b. Theoretical background

The classical linear mechanism of baroclinic instability considered by Charney (1947) and Eady (1949)

* Current address: Marine Sciences Program, University of North Carolina at Chapel Hill, Chapel Hill, North Carolina.

Corresponding author address: Dr. Huijie Xue, University of North Carolina at Chapel Hill, Marine Sciences Program, CB #3300, 12-5 Venable Hall, Chapel Hill, NC 27599-3300.

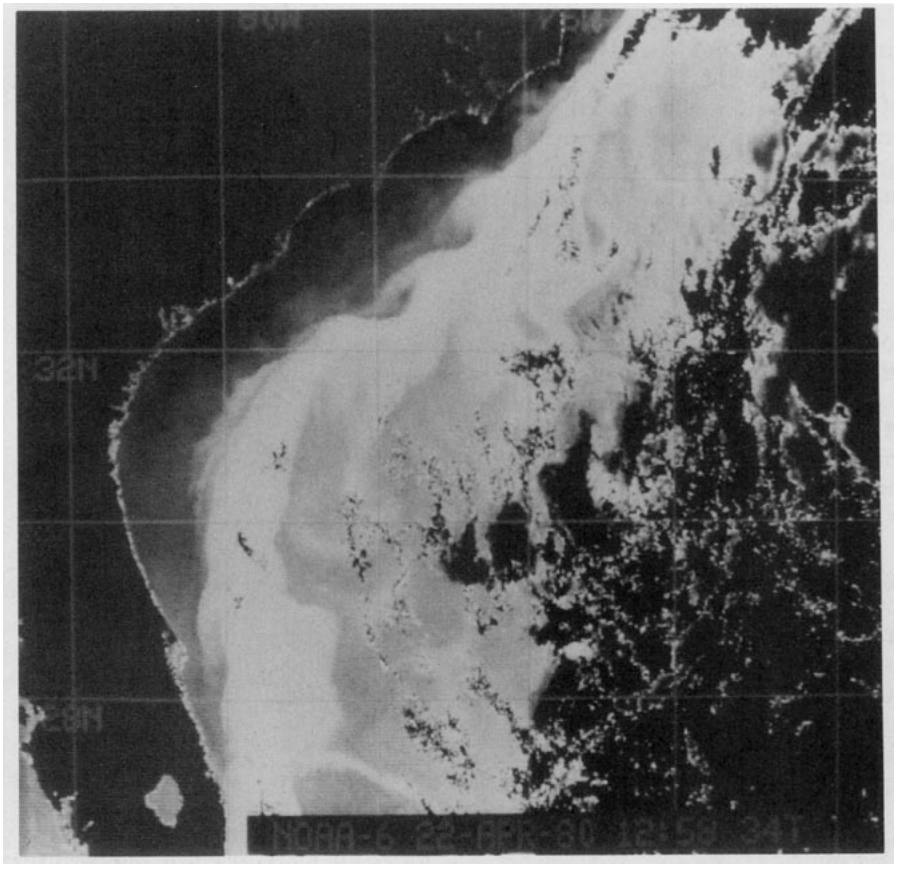

FIG. 1. Satellite thermal image on 22 April 1980 showing meanders in the South Atlantic Bight. (Image courtesy of O. Brown and R. Evans, University of Miami.)

explained the fact that growing disturbances both in the atmosphere and in oceans have preferred scales. Blumsack and Gierasch (1972) included the effect of a uniform sloping bottom in the Eady model. In addition to the short-wave cutoff, they found a long-wave cutoff. The most important result was that the flow becomes stable if the bottom slope exceeds the isopycnal slope. Johns (1988) considered the interplay of the vertical variations of the potential vorticity gradient and the bottom slope in his study of the Gulf Stream near 74°W. He found that the unstable waves are sensitive to the depth where the potential vorticity gradient changes from positive to negative. The major effect of the bottom slope was a decrease of growth rate at low frequencies. McIntyre (1970) solved a perturbed Eady problem in which both horizontal and vertical gradients operate simultaneously. He concluded that there is instability at short wavelengths.

By including nongeostrophic effects, Stone (1966) found three types of instabilities associated with different ranges of Richardson number, and later (Stone 1970), he found a secondary unstable branch that had a shorter wavelength compared with Eady waves. Moore and Peltier (1987) solved linearized primitive equations to test stability of two-dimensional atmospheric fronts. A combined method of Fourier–Galerkin and orthogonal collocation is used in their spectral model. In addition to a long wavelength Charney–Eady mode of baroclinic instability, they successfully captured the preferred scale of cyclogenesis in the atmosphere. Unlike the Charney–Eady waves, the new mode found in their model was confined to the bottom boundary. Their subsequent papers (Moore and Peltier 1989a,b) showed that quasigeostrophic theory not only failed to account for the unstable, cyclone-scale mode, it also rather severely distorted the long wavelength Charney–Eady mode. The geostrophic momentum approximation similarly filtered the cyclone-scale mode, but it corrected the phase speed and growth rate errors for the long waves that were introduced by the quasigeostrophic approximation.

The development of frontal eddies along oceanic boundary currents is more complicated due to the presence of the coastline and the bottom slope. In the application of his two-layer model to the Gulf Stream, Orlanski (1969) demonstrated that topographical slope is a stabilizing factor, while the height of the topography is a destabilizing factor. However, his prescribed cross

section had little resemblance to the Gulf Stream in the SAB, and his two-layer model did not provide enough vertical resolution, which is crucial because of the sensitivity of the dispersion relation to the vertical profile of the mean potential vorticity gradient (Johns 1988). Luther and Bane (1985) regarded Gulf Stream meanders as spatially growing waves. They forced the system with a wind stress and solved for resonant responses.

In the present study, the method used by Moore and Peltier (1987) is adopted with the following modifications: 1) a coordinate transformation to map the cross section with topography to a rectangular domain, 2) different basis functions to fit the boundary condition at the coast, and 3) a new approach to calculate the barotropic pressure. (They used a nonhydrostatic relation for barotropic pressure that was inconsistent with the hydrostatic approximation used elsewhere in their analysis.)

The following section describes procedures to form the eigenvalue problem for the instability study of the Gulf Stream. In section 3, we propose two analytical cross sections to represent the mean conditions of the Gulf Stream upstream and downstream of the Charleston Bump. Section 4 is the application of the model to the Gulf Stream front. Two cases, with or without topography, have been analyzed for each cross section. Section 5 discusses the stabilizing mechanism of the bottom topography and mechanisms of unstable short waves. Conclusions are given in section 6.

2. Formulation of an eigenvalue problem

a. The basic equations

A straight coastline is stipulated along the y axis, with the x axis positive in the offshore direction and the z axis positive upward (Fig. 2). A steady current, $V(x, z)$, flows parallel to the coast, which is in thermal wind balance with a mean density field, $\rho(x, z)$, according to $fV_z = B_x$. Here B is the buoyancy of the mean state defined as $B = -g\rho(x, z)/\rho_0$, where ρ_0 is a reference density. All quantities related to the mean flow are uniform in y but nonseparable functions of x and z. We consider perturbed motions linearly superimposed on the mean state in a hydrostatic, Boussinesq fluid. A middle-latitude $f$plane is used. Equations governing the evolution of the perturbations in conventional Cartesian coordinates are

$$\frac{\partial u}{\partial t} + V\frac{\partial u}{\partial y} - fv = -\frac{\partial \pi}{\partial x} \quad (2.1a)$$

$$\frac{\partial v}{\partial t} + V\frac{\partial v}{\partial y} + fu + uV_x + wV_z = -\frac{\partial \pi}{\partial y} \quad (2.1b)$$

$$b = \frac{\partial \pi}{\partial z} \quad (2.1c)$$

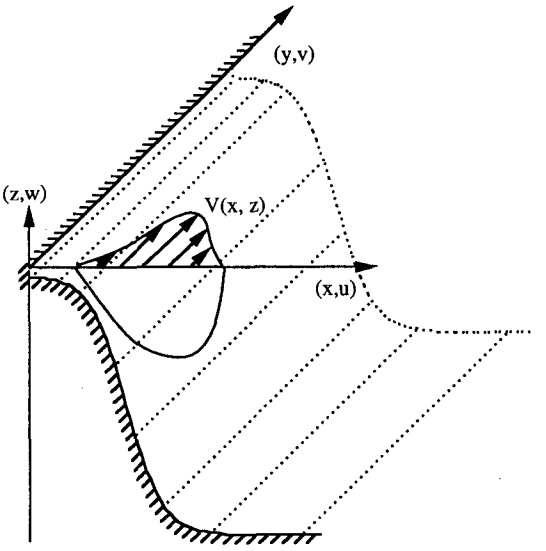

FIG. 2. Schematic of model geometry.

$$\frac{\partial u}{\partial x} + \frac{\partial v}{\partial y} + \frac{\partial w}{\partial z} = 0 \quad (2.1d)$$

$$\frac{\partial b}{\partial t} + V\frac{\partial b}{\partial y} + uB_x + wB_z = 0. \quad (2.1e)$$

The (x, y, z) components of the perturbation velocity are (u, v, w); π is the perturbation pressure divided by ρ_0, b is the perturbation buoyancy. Boundary conditions are required to close the problem posed by (2.1). Normal flow at the solid boundaries is null, and the rigid-lid approximation is stipulated. Furthermore, disturbances vanish at distances far from the coast. Thus,

$$u = 0 \quad \text{at} \quad x = 0 \quad \text{and}$$
$$\pi, u \text{ and } v \to 0 \quad \text{as} \quad x \to \infty \quad (2.2a)$$

$$w = 0 \quad \text{at} \quad z = 0 \quad \text{and}$$
$$w = -u\frac{\partial h}{\partial x} \quad \text{at} \quad z = -h(x). \quad (2.2b)$$

A "sigma coordinate" mapping is applied to transform the complicated cross section to a rectangular one to facilitate the application of vertical boundary conditions and the choice of basis functions. The coordinate transformation and a new vertical velocity, ω, are

$$\zeta = 1 + z/h(x) \quad (2.3a)$$

$$\omega = w - (\zeta - 1)u\frac{\partial h}{\partial x}. \quad (2.3b)$$

Then, the transport form of variables u^*, v^*, and b^* is used such that

$$(u^*, v^*, b^*) = (uh, vh, bh). \quad (2.4)$$

Finally, the problem will be solved in dimensionless form. All quantities are scaled by their reference values as follows:

$$(x', y') = (x, y)/L_0, \quad \zeta' = \zeta, \quad t' = tf, \quad h' = h/H_0$$
$$(u', v') = (u^*, v^*)/u_0, \quad \omega' = (L_0/u_0)\omega$$
$$\pi' = (H_0/u_0 f L_0)\pi, \quad b' = (H_0/u_0 f L_0)b^*$$
$$B' = B/H_0 N_0^2, \quad V' = V/V_0, \qquad (2.5)$$

where L_0 is the horizontal length scale and H_0 the vertical length scale, u_0 is the typical perturbation velocity times H_0, V_0 is the maximum of V, and N_0^2 the maximum of the vertically averaged B_z. Since the mean field variables in (2.1) depend only on x and ζ, one can assume that the solutions have the following functional form:

$$(u', \omega') = \mathrm{Re}[(\tilde{u}(x, \zeta), \tilde{\omega}(x, \zeta))e^{i(\sigma t+\beta y)}] \qquad (2.6a)$$

$$(v', \pi', b') = \mathrm{Re}[(i\tilde{v}(x, \zeta), i\tilde{\pi}(x, \zeta), i\tilde{b}(x, \zeta))e^{i(\sigma t+\beta y)}]. \qquad (2.6b)$$

Here β is the alongfront wavenumber and $\sigma = \sigma_r + i\sigma_i$, where $-\sigma_i$ is the growth rate; a disturbance is said to be unstable if $\sigma_i < 0$; σ_r is the wave frequency; the phase speed is given by $-\sigma_r/\beta$; Re[ ] denotes the real part of the expression in the bracket. Including i in the right-hand side of (2.6b) yields a set of equations with all real coefficients. Substituting (2.3), (2.4), and (2.5) into (2.1), one obtains the following equations:

$$(\sigma + \mathrm{Ro}\beta V)\tilde{u} - \tilde{v} = -h\frac{\partial \tilde{\pi}}{\partial x} + (\zeta - 1)\frac{\partial h}{\partial x}\tilde{b} \qquad (2.7a)$$

$$(\sigma + \mathrm{Ro}\beta V)\tilde{v} - \tilde{u} - \mathrm{Ro}V_x\tilde{u} - \mathrm{Ro}V_\zeta\tilde{\omega} = -\beta h\tilde{\pi} \qquad (2.7b)$$

$$\tilde{b} = \frac{\partial \tilde{\pi}}{\partial \zeta} \qquad (2.7c)$$

$$\frac{\partial \tilde{u}}{\partial x} - \beta\tilde{v} + \frac{\partial \tilde{\omega}}{\partial \zeta} = 0 \qquad (2.7d)$$

$$(\sigma + \mathrm{Ro}\beta V)\tilde{b} - SB_x\tilde{u} - SB_\zeta\tilde{\omega} = 0, \qquad (2.7e)$$

where $\mathrm{Ro} = V_0/fL_0$ is the Rossby number of the mean flow, $S = N_0^2H_0^2/(f^2L_0^2)$. The boundary conditions are

$$\tilde{u} = 0 \quad \text{at} \quad x = 0 \quad \text{and}$$
$$(\tilde{u}, \tilde{v}, \tilde{\omega}, \tilde{\pi}, \tilde{b}) \to 0 \quad \text{as} \quad x \to \infty \qquad (2.8a)$$
$$\tilde{\omega} = 0 \quad \text{at} \quad \zeta = 0 \quad \text{and} \quad \text{at} \quad \zeta = 1. \qquad (2.8b)$$

b. Numerical formulation

Galerkin and collocation schemes are applied to solve the problem described by (2.7) and (2.8). In the Galerkin approach, weighting functions are the same as the basis functions, which individually satisfy the boundary conditions. In the collocation approach, weighting functions are Dirac delta functions centered at collocation points. The choice of basis functions is important in order to obtain accurate solutions. Generally speaking, a good choice will take into account the boundary conditions. For example, a modified Laguerre polynomial could be chosen for the Dirichlet problem in a semi-infinite domain (Mellor 1962). However, there are two additional ways to construct global approximations to functions defined on a semi-infinite domain: 1) map the semi-infinite domain into a finite one and 2) truncate the domain to $[0, L]$. When the last approach is used, exponential convergence can be achieved only by increasing L while increasing the truncation level (Boyd 1982).

In the present study, the Fourier–Galerkin method is applied in the vertical with the exception of the thermodynamic equation (2.7e), where, for reasons discussed later, Fourier collocation is used. In the cross-front direction the domain is truncated at $x = L$ and the Fourier–Galerkin method is applied. This is equivalent to forming the problem in a channel with the expectation that if the channel is wide enough, the waves spanning the channel do not affect the unstable modes trapped along the front. Structure functions, $\{\tilde{u}, \tilde{v}, \tilde{\omega}, \tilde{b}\}$, are spectrally decomposed into orthogonal sets of basis functions in the vertical:

$$(\tilde{u}, \tilde{v}, \tilde{\pi}) = \sum_{\nu=0}^{N} (u_\nu(x), v_\nu(x), p_\nu(x))E_\nu \qquad (2.9a)$$

$$(\tilde{\omega}, \tilde{b}) = \sum_{\nu=1}^{N} (\omega_\nu(x), b_\nu(x))F_\nu \qquad (2.9b)$$

$$E_\nu = \cos(\nu\pi\zeta) \quad \text{and} \quad F_\nu = \sin(\nu\pi\zeta), \qquad (2.9c)$$

where N is the truncation level. Substituting these expansions into Eqs. (2.7) results in a set of residual equations, with the residuals consisting of wave components that exceed the truncation level N (details are provided in appendix A). It is required that each of the residuals is orthogonal to a set of weighting functions. Weighting functions for prognostic equations are chosen so that the terms involving the eigenvalue, σ, are diagonal. Those for the diagnostic equations are chosen so that the terms involving ω and p are diagonal. However, before deciding on the weighting functions, one should understand the implication of the expansions given by (2.9): the expansion for $\tilde{\omega}$ satisfies the boundary conditions (2.8), while the expansions for $\tilde{u}$, $\tilde{v}$, and $\tilde{\pi}$ imply that

$$\frac{\partial \tilde{u}}{\partial \zeta} = \frac{\partial \tilde{v}}{\partial \zeta} = \frac{\partial \tilde{\pi}}{\partial \zeta} = 0 \quad \text{at} \quad \zeta = 0 \quad \text{and} \quad \zeta = 1. \qquad (2.10)$$

Strictly speaking, one cannot specify vertical boundary conditions for quantities other than the vertical velocity. Therefore, (2.10) overconstrains the problem at $\zeta = 0$ and $\zeta = 1$, so that error is incurred

within the region of $0 \leqslant \zeta < \epsilon$ and $1 - \epsilon < \zeta \leqslant 1$; however, ϵ decreases as the truncation level increases. Furthermore, it has been shown in Moore and Peltier (1987) that by comparing the result of the Galerkin method, which uses these boundary conditions, with the result of the shooting method, which does not, one can apply these approximate boundary conditions without affecting the interior solution significantly. Therefore, the spectral weighting method is applied to (2.7a,b,c, and d). However, there are difficulties in the density equation (2.7e). The expansion of $\tilde{b}$ implies

$$\tilde{b} = 0 \quad \text{at} \quad \zeta = 0 \quad \text{and} \quad \zeta = 1. \tag{2.10a}$$

On the other hand, (2.7e) implies

$$(\sigma + \mathrm{Ro}\beta V)\tilde{b} - SB_x\tilde{u} = 0 \quad \text{at} \quad \zeta = 0 \quad \text{and} \quad \zeta = 1. \tag{2.10b}$$

It is clear that (2.10a) and (2.10b) are inconsistent when B_x is not zero at the upper and lower boundaries. Moore and Peltier (1987) found that expansions given in (2.9) result in unacceptable "Gibbs" behavior in the structure function, $\tilde{b}$, in the interior of the domain. The Gibbs oscillations can be suppressed by increasing the truncation level. However, they found that these oscillations can be avoided entirely by applying the orthogonal collocation method to the density equation. Following Moore and Peltier (1987), the pseudo-spectral weighting functions are chosen to be a set of Dirac delta functions with collocation points equally spaced within the interval (0, 1):

$$H_\gamma = \delta(\zeta - \zeta_\gamma) \tag{2.11a}$$

$$\zeta_\gamma = \frac{\gamma}{N+1}, \quad \gamma = 1, 2, \cdots, N. \tag{2.11b}$$

Note that $0 < \zeta_\gamma < 1$; therefore, the residual is never evaluated at $\zeta = 0$ and $\zeta = 1$, and the apparent over-constraint of $\tilde{b}$ at $\zeta = 0$ and 1 is avoided.

Each residual equation, formed from (2.7) and listed in (A.1), is multiplied by the weighting functions E_μ, F_μ, or H_μ and is integrated vertically from 0 to 1. Taking advantage of the orthogonality of the trigonometric functions, one obtains the following differential equations:

$$\sigma u_\mu = -(\mathrm{Ro}\beta/(1+\delta_{\mu 0}))\langle E_\mu V E_\nu\rangle u_\nu + \delta_{\mu\nu}v_\nu - h\delta_{\mu\nu}\frac{\partial p_\nu}{\partial x} + (1/(1+\delta_{\mu 0}))\langle E_\mu(\zeta-1)F_\nu\rangle\frac{\partial h}{\partial x}b_\nu \tag{2.12a}$$

$$\sigma v_\mu = \delta_{\mu\nu}u_\nu + \mathrm{Ro}/(1+\delta_{\mu 0})\{\langle E_\mu V_x E_\nu\rangle u_\nu - \beta\langle E_\mu V E_\nu\rangle v_\nu + \langle E_\mu V_\zeta F_\nu\rangle\omega_\nu\} - \beta h\delta_{\mu\nu}p_\nu \tag{2.12b}$$

$$\sigma b_\mu = SC^{-1}_{\mu\gamma}2\cos(\nu\pi\zeta_\gamma)B_x(x,\zeta_\gamma)u_\nu + SC^{-1}_{\mu\gamma}2\sin(\nu\pi\zeta_\gamma)B_\zeta(x,\zeta_\gamma)\omega_\nu - \mathrm{Ro}\beta C^{-1}_{\mu\gamma}2\sin(\nu\pi\zeta_\gamma)V(x,\zeta_\gamma)b_\nu \tag{2.12c}$$

$$p_\mu = -b_\mu/\mu\pi \quad \text{for} \quad \mu \geqslant 1 \tag{2.13a}$$

$$\omega_\mu = -\frac{1}{\mu\pi}\left\{\frac{\partial u_\mu}{\partial x} - \beta v_\mu\right\} \quad \text{for} \quad \mu \geqslant 1. \tag{2.13b}$$

Here, the operator $\langle\ \rangle$ is defined as $\langle\aleph\rangle = 2\int_0^1 \aleph d\zeta$; the repeated subscript, ν, represents summation from 0 to N; $C_{\gamma\nu} = 2\sin(\nu\pi\zeta_\gamma)$, and $C^{-1}_{\mu\gamma}C_{\gamma\nu} = \delta_{\mu\nu}$. Each of the prognostic equations in (2.12) has a term with the coefficient, σ, and together, they form a linear eigenvalue problem. The two diagnostic equations in (2.13) will be used to eliminate ω and p from the prognostic equations. Notice that the barotropic pressure, p_0, is excluded from (2.13a). In rigid-lid models, internal modes are driven only by the baroclinic pressure gradient, and they can be calculated independent of p_0. The external mode can be obtained from the following set of equations:

$$\frac{\partial u_0}{\partial x} - \beta v_0 = 0 \tag{2.14a}$$

$$\sigma u_0 = -0.5\mathrm{Ro}\beta\langle E_0 V E_0\rangle u_0 + \frac{1}{\beta}\frac{\partial u_0}{\partial x} - h\frac{\partial p_0}{\partial x} - 0.5\mathrm{Ro}\beta\langle E_0 V E_\nu\rangle u_\nu + 0.5\langle E_0(\zeta-1)F_\nu\rangle\frac{\partial h}{\partial x}b_\nu \tag{2.14b}$$

$$\sigma v_0 = u_0 + 0.5\mathrm{Ro}\left\{\langle E_0 V_x E_0\rangle u_0 - \langle E_0 V E_0\rangle\frac{\partial u_0}{\partial x}\right\} + 0.5\mathrm{Ro}\left\{\langle E_0 V_x E_\nu\rangle u_\nu - \frac{1}{\nu\pi}\langle E_0 V_\zeta F_\nu\rangle\frac{\partial u_\nu}{\partial x}\right\} - 0.5\mathrm{Ro}\beta\left\{\langle E_0 V E_\nu\rangle - \frac{1}{\nu\pi}\langle E_0 V_\zeta F_\nu\rangle\right\}v_\nu - \beta h p_0. \tag{2.14c}$$

Equation (2.14a) is obtained by integrating the continuity equation, (2.13b), from the bottom to the top. Equations (2.14b) and (2.14c) are obtained from (2.12a) and (2.12b) when $\mu = 0$. A diagnostic equation for p_0 can be obtained by cross differentiating (2.14b) and (2.14c) and can be used to solve for p_0. Substituting p_0 into (2.14b) and combining with the internal-mode equations yields a complete set of equations for determining frontal instability.

One can either solve the equation set by means of horizontal differencing or by a spectral transform in

the horizontal. We follow the latter procedure so that $\{u_\mu, v_\mu, b_\mu, u_0, p_0\}$, are spectrally expanded horizontally using trigonometric functions:

$$(u_0, u_\nu) = \sum_{\lambda=1}^{\infty} (u_{\lambda 0}, u_{\lambda\nu})\psi_\lambda \qquad (\nu = 1, 2, \cdots, N) \quad (2.15a)$$

$$\{p_0, v_\nu, b_\nu\} = \sum_{\lambda=0}^{\infty} \{(p_{\lambda 0}, v_{\lambda\nu}, b_{\lambda\nu})\phi_\lambda\} \qquad (\nu = 1, 2, \cdots, N) \quad (2.15b)$$

$$\phi_\lambda = \cos\frac{\lambda\pi x}{L} \quad \text{and} \quad \psi_\lambda = \sin\frac{\lambda\pi x}{L}. \quad (2.15c)$$

Using the orthogonal relationships, the diagnostic equation for p_0 and (2.12) become

$$p_{\kappa 0} = P^{-1}_{\kappa\gamma} \cdot \{J^1_{\gamma 0\lambda\nu} u_{\lambda 0} + J^2_{\gamma 0\lambda\nu} u_{\lambda\nu} + J^3_{\gamma 0\lambda\nu} v_{\lambda\nu} + J^4_{\gamma 0\lambda\nu} b_{\lambda\nu}\} \quad (2.16)$$

$$\sigma u_{\kappa\mu} = M^1_{\kappa\mu\lambda\nu} u_{\lambda\nu} + M^2_{\kappa\mu\lambda\nu} v_{\lambda\nu} + M^3_{\kappa\mu\lambda\nu} b_{\lambda\nu} \quad (2.17a)$$

$$\sigma v_{\kappa\mu} = M^4_{\kappa\mu\lambda\nu} u_{\lambda\nu} + M^5_{\kappa\mu\lambda\nu} v_{\lambda\nu} + M^6_{\kappa\mu\lambda\nu} b_{\lambda\nu} \quad (2.17b)$$

$$\sigma b_{\kappa\mu} = M^7_{\kappa\mu\lambda\nu} u_{\lambda\nu} + M^8_{\kappa\mu\lambda\nu} v_{\lambda\nu} + M^9_{\kappa\mu\lambda\nu} b_{\lambda\nu}, \quad (2.17c)$$

where $P^{-1}_{\kappa\gamma}$, $J^1_{\gamma 0\lambda\nu}$, $J^2_{\gamma 0\lambda\nu}$, $J^3_{\gamma 0\lambda\nu}$, $J^4_{\gamma 0\lambda\nu}$, and $M^1_{\kappa\mu\lambda\nu}, \ldots, M^9_{\kappa\mu\lambda\nu}$ are defined in appendix A. A triangular truncation scheme ($\mu = 0, 1, \cdots, N$; $\kappa = 0, 1, \cdots, N - \mu$) is used to truncate the Galerkin expansions. To place the reduced eigen system into a standard form, a mapping routine is used to organize wavenumbers (κ, μ) into an increasing sequence. This allows one to order the two-dimensional coefficients $(u_{\kappa\mu}, v_{\kappa\mu}, b_{\kappa\mu})$ into a one-dimensional vector, $\mathbf{X}_i$, and to arrange the four-dimensional matrix elements, $M^1_{\kappa\mu\lambda\nu}$ to $M^9_{\kappa\mu\lambda\nu}$, into a two-dimensional matrix, $\mathbf{E}_{ij}$. The detailed mapping procedures are provided in appendix B. The procedure results in a standard matrix eigenvalue problem,

$$\mathbf{E}_{ij}\mathbf{X}_j = \sigma\mathbf{X}_i. \quad (2.18)$$

With a prescribed mean flow, whenever a wavenumber is specified, (2.18) is solved by calling the subroutine EVCRG in the IMSL library (version 1.1, 1989) to obtain the eigen solutions. The number of elements in the matrix grows proportional to the square of the truncation level so that the model can be computationally expensive if a high truncation level is required. Appendix C provides formulas to construct mode structures in physical space and to diagnose energy budgets of the unstable modes. Appendix D is an application of the model to stable waves in a channel, which is used to verify the model.

3. Mean state of the Gulf Stream front

In the present study, analytic formulas are provided to approximate the mean condition of the Gulf Stream. The bottom topography in the SAB generally consists of a wide continental shelf and a sharp continental slope, which is approximated by a hyperbolic tangent function in the model:

$$h(x) = H_s + \frac{1}{2}(H_d - H_s)\left\{1 + \tanh\frac{x - x_m}{\alpha}\right\}. \quad (3.1)$$

Here H_s is the depth over the shelf, and H_d is the maximum depth in the domain. The slope is determined by α, and the location of the maximum slope is determined by x_m.

There were several multiyear experiments measuring the downstream velocity and temperature of the Gulf Stream in the SAB. Richardson et al. (1969) showed direct transport measurements by dropsondes along sections between the Florida Keys and Cape Fear during 1965–68. They found that the transport increased from 29.6 Sv off the Florida Keys to approximately 53 Sv off Cape Fear. For all sections, the mean current had a single maximum at each depth, and the location of the maximum velocity shifts offshore with increasing depth. Vertical shears of the downstream velocity are small on the offshore side of the stream. There were no temperature measurements in this experiment. More recently, using the data collected by PEGASUS during the Sub-Tropical Atlantic Climate Studies, the Florida Atlantic Coast Transport Study, and the Cape Hatteras Experiment, Leaman et al. (1989) showed the average velocity and temperature of the Gulf Stream at 27°N, 29°N and off Cape Hatteras. Velocity distributions were similar to those in Richardson et al. (1969). Temperature was approximately in geostrophic balance with the downstream velocity. The so-called 18° Water appears on the offshore side of the Gulf Stream between 300 and 500 m.

To reproduce observed structures of the Gulf Stream, the following analytic formula of downstream velocity is used; then a relationship between the horizontal gradient of the buoyancy field and the vertical derivative of the velocity is established according to the thermal-wind balance:

$$V(x, z) = V_0 \exp\left\{\frac{z}{z_s} - X_i^2\right\} \quad (3.2)$$

$$B_x(x, z) = \frac{fV_0}{z_s}\left\{1 - 2X_i\left(\frac{x_f A_0}{x_d A^2} - X_i\frac{z_s}{x_d}\frac{dx_d}{dz}\right)\right\} \times \exp\left\{\frac{z}{z_s} - X_i^2\right\} \quad (3.3)$$

where

$$X_i = X_i(x) = \left[x - x_f\left(1 - \frac{z}{z_s \cdot A}\right)\right] \Big/ x_d \quad (3.4)$$

$$A = A_0 + 2z/H_d \quad (3.5)$$

$$\left[x_d, \frac{dx_d}{dz}\right] = \begin{cases} x_{d1} - \dfrac{z(x_{d2} - x_{d1})}{H_d}, \\ \qquad - \dfrac{x_{d2} - x_{d1}}{H_d} \quad \text{if} \quad X_i \leqslant 0 \\ x_{d2}, \quad 0 \quad \text{if} \quad X_i > 0. \end{cases} \tag{3.6}$$

Here, V_0 is the maximum velocity of the current, x_f defines the location of the surface velocity maximum, x_d defines the width of the current, z_s determines the velocity decreasing rate against depth, and A determines the eastward tilt of the maximum velocity as depth increases. To obtain $B(x, z)$, (3.3) is integrated numerically. The integration begins at the eastern boundary since isotherms there are nearly flat. The presence of the Blake Plateau upstream of the Charleston Bump results in considerably different topography compared to that off Onslow Bay. Therefore, two sets of values are given in Table 1 to form cross sections in regions upstream and downstream of the Charleston Bump, respectively; see Figs. 3a and 3b. The maximum depth is smaller, but the slope is steeper upstream of the Bump. In addition to the difference in topography, the Gulf Stream transport increases between the Florida Keys and Cape Hatteras despite the slight decrease of the core velocity.

The Gulf Stream given in Figs. 3a and 3b has features similar to those observed by Richardson et al. (1969) and Leaman et al. (1989). For example, the mean current has only one maximum at each depth; the positions of the maximum velocity at each level shift eastward as depth increases; on the eastern side of the current, the vertical gradient is almost zero near the surface. The stream decelerates at the surface from cross section I to cross section II, but it tends to increase both the width and the depth. The increase of total transport from 32 Sv to 52 Sv agrees with the observations. The decrease of the vertical density gradient around 400-m depth indicates the location of the 18° Water.

At each cross section, two frontal zones are examined; I_0 and I_1 denote the frontal zones using the mean condition at cross section I with and without a bottom slope. Similar definitions are denoted by II_0 and II_1 at cross section II. Scale quantities used in equation (2.5) associated with both cross sections are given in Table 2. Numerical solutions of (2.18) for each front yield the growth rate and phase speed spectra, $-\sigma_i(\beta)$ and

TABLE 1. Quantities used to generate Figs. 3a and 3b. The scale of H_s, H_d, and z_s is in meters; the scale of α, x_m, x_f, x_{d1}, and x_{d2} is in kilometers; and the scale of V_0 is in meters per second.

Cross section	H_s	H_d	α	x_m	V_0	A_0	z_s	x_f	x_{d1}	x_{d2}
I	50	900	20	110	1.9	3.0	300	110	20	45
II	100	3000	55	150	1.7	5.0	450	120	28	50

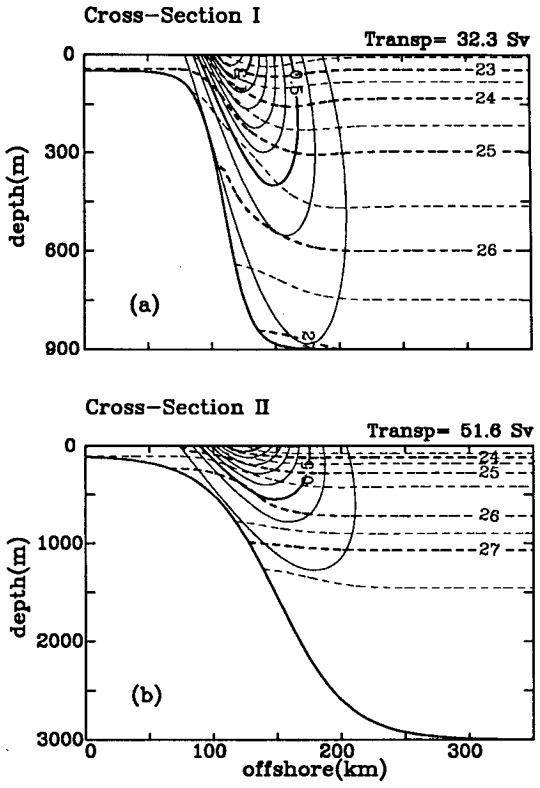

FIG. 3. Gulf Stream frontal zones in the South Atlantic Bight. Solid contours are velocity; contour interval is 0.2 m s^{-1}. Dashed contours are isopycnals; contour interval is 0.5 kg m^{-3}. (a) Cross section I represents the Gulf Stream between Cape Canaveral and Charleston; (b) cross section II represents the Gulf Stream between Charleston and Cape Hatteras.

$C_{ph}(\beta) = -\sigma_r(\beta)/\beta$, as functions of alongfront wavenumber, as well as the corresponding mode structures. Discussion will be restricted to the first three unstable modes.

4. Instability of the Gulf Stream front

a. Convergence of the model

One fundamental problem of spectral models is to find the rate at which a truncated solution u_N converges to the real solution u and to estimate the error $\|u - u_N\|$. However, for numerical calculations, one can only determine an appropriate N at which $\|u_{N+1} - u_N\|$ is less than a given small number. Several factors can affect the convergence rate, such as the truncation of the offshore domain limit and the alongfront wavenumber. Of course, when the model is applied to different frontal zones, it may converge at different speeds; $\epsilon = 0.002$ is chosen, which is less than 5% of the eigenvalues (growth rates in the present problem). The truncation level N is determined according to

$$\|\sigma_i|_{n+1} - \sigma_i|_n\| \leqslant \epsilon \quad \text{for} \quad n = N - 1, N, N + 1. \tag{4.1}$$

TABLE 2. Scaling quantities used in (2.5) and resulting dimensionless parameters in (2.7).

Cross section	$f(\text{sec}^{-1})$	H_0 (m)	L_0 (km)	V_0 (m s^{-1})	N_0^2 (s^{-2})	Ro	S
I	7.27×10^{-5}	900	100	1.9	5.56×10^{-5}	0.261	0.852
II	7.79×10^{-5}	3000	100	1.7	1.53×10^{-5}	0.218	2.269

The required computing resource increases very quickly as the truncation level goes up. For example, it takes less than 1 second to solve equation (2.18) at each given wavenumber when $N = 10$, approximately 20 seconds when $N = 20$, and approximately 350 seconds when $N = 30$. First, the larger the alongfront wavenumber is, the higher the truncation level should be. Second, there is a general tendency of slower convergence as L increases. Third, the front in cross section II is wider compared to that in cross section I; thus, a larger L and a higher truncation level might be beneficial. Nevertheless, $L = 3.5$ and $N = 28$ are chosen for all four frontal zones in the present study. Although, as seen in Fig. 4, the convergence at short waves is not as good as that at long waves, we think it is acceptable even at wavenumber 7.0. Figure 5 shows the amplitude of the perturbed velocity component, u, of the most unstable mode at three different truncation levels. It also indicates that $N = 28$ is sufficient to obtain a converged solution.

b. *The cross section upstream of the Charleston Bump*

Figures 6a and 6b display the growth rate and the corresponding phase speed spectra of the first two unstable modes on the front, I_0. The growth rate spectra for long waves are similar to those of the classical unstable Charney–Eady waves, whereas they are considerably different at short waves as nongeostrophic effects become more important. Like most nongeostrophic models, there are unstable solutions at short waves. Stone (1970) found similar unstable branches for Richardson number less than 2. He also mentioned that these branches may still exist when the Richardson number is greater than 2, but their growth rates were so small that they fell within the error range of his analysis. In the present study, even though the Richardson number, $N_0^2 H_0^2 / V_0^2$, is the order of 10, short-wave branches can still be clearly identified. The reason is that the horizontal gradients of the Gulf Stream front also generate unstable short waves as seen in McIntyre (1970).

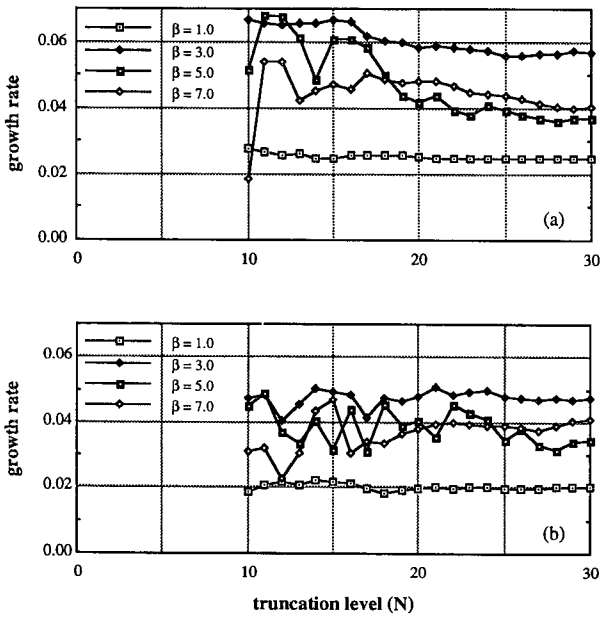

FIG. 4. Convergence of the model at different alongfront wavenumbers: (a) results from the front zone I_1, and (b) results from front zone II_1; *wn* is the nondimensional wavenumber, β.

The first mode, m_1, has the most unstable wave at the alongfront wavenumber 3.4 with a nondimensional growth rate of 0.088, which is equivalent to a dimensional wavelength of 185 km and an *e*-folding time scale of 1.8 days. The growth rate of m_1 reduces slowly on the short-wave side. The second mode, m_2, has two branches separated at wavenumber 5.0. On the long-wave side, the maximum growth rate of 0.052 occurs at wavenumber 4.1; on the short-wave side, the maximum growth rate of 0.062 occurs at wavenumber 7.5. It is clear that m_2 has the largest growth rate among short waves. Generally speaking, longer waves move at slower speeds. The phase speed of the m_1 increases quickly on the long-wave side and changes very little on the short-wave side. The most unstable wave at wavenumber 3.4 has a phase speed of about 0.049, which corresponds to a dimensional propagation speed of 30.8 km day^{-1}; m_2 moves almost three times as fast as m_1, and its phase speed increases linearly as the wavenumber increases except for a small jump at wavenumber 5.0 where the growth rate spectrum of the m_2 reaches a minimum. The most unstable wave of the m_2 has a phase speed of 0.177.

The growth rate and phase speed spectra with respect to front I_1 are given in Fig. 7. It is obvious that topography is a stabilizing factor. The reduction of the growth rate is 38% for the first mode and 30% for the second. A secondary effect of the topography is the shift of the growth rate spectra toward long waves. The maximum growth rate of m_1 is 0.055, occurring at wavenumber 3.0 in this case, which corresponds to a dimensional wavelength of 215 km and an *e*-folding time scale of 2.9 days; m_2 is once again dominant among short waves: it has the maximum growth rate of 0.042 at

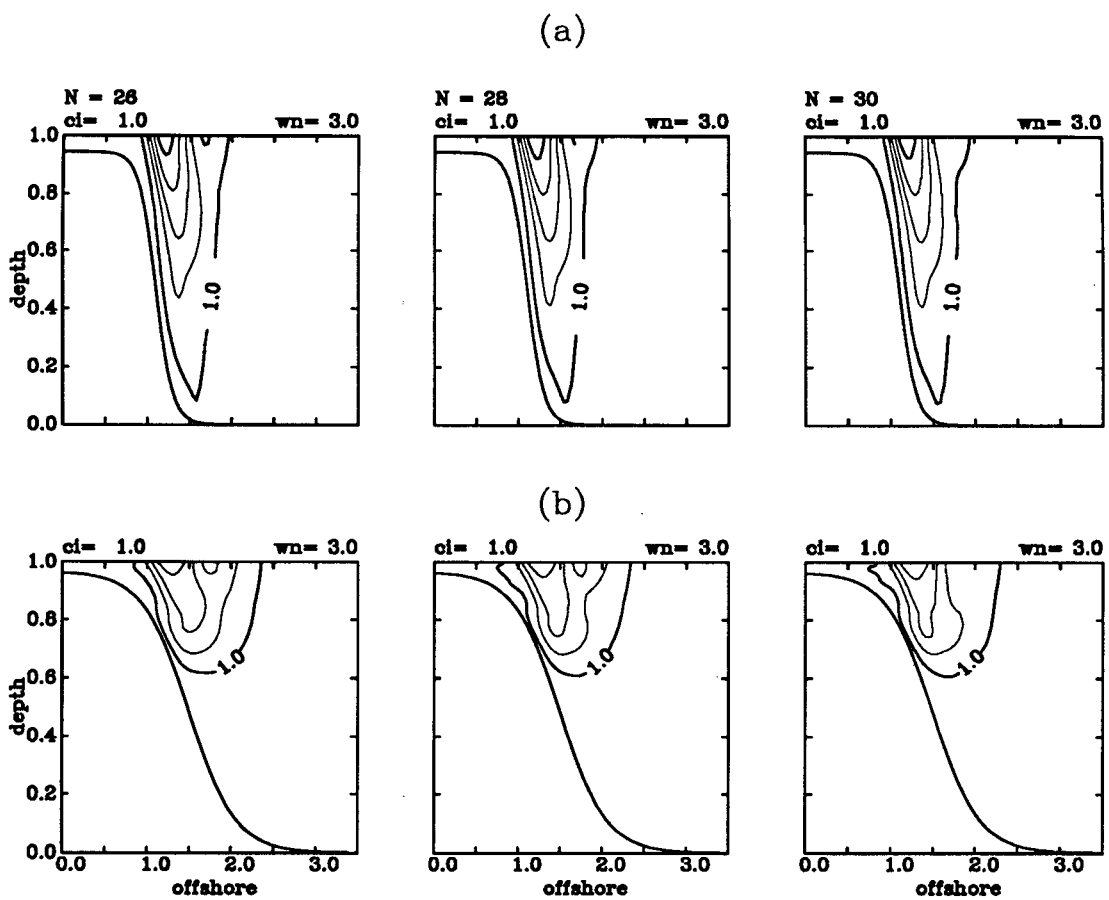

FIG. 5. Amplitude of perturbation velocity component u of the first unstable mode at three different truncation levels: (a) is for frontal zone I_1; (b) is for frontal zone II_1.

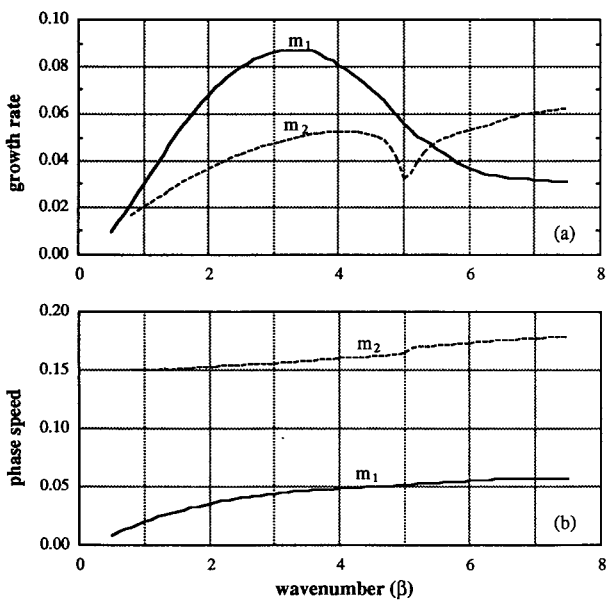

FIG. 6. Growth rate spectra (a) and phase speed spectra (b) of the two most unstable modes growing on front I_0, a flat bottom case. All quantities are nondimensionalized according to (2.5).

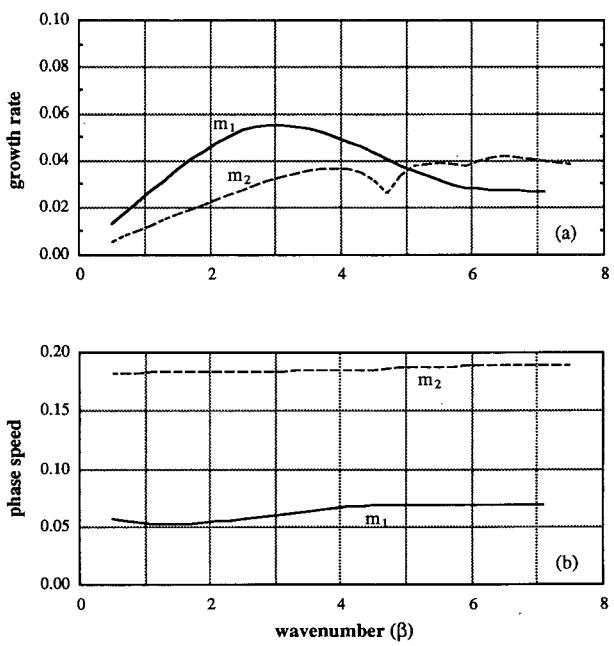

FIG. 7. As in Fig. 6 except for front I_1, with bottom topography.

wavenumber 6.5. The overall topographic effect on phase speeds is the increase of phase speeds, especially at long waves so that both m_1 and m_2 become less dispersive. The phase speed of the most unstable wave at wavenumber 3.0 reaches 0.062, which corresponds to a dimensional propagation speed of 39.3 km day^{-1}. The phase speed of m_2 is almost three times the phase speed of m_1 at all wavenumbers.

Structure functions of m_1 and m_2 are given in Fig. 8 and Fig. 9, respectively. All unstable modes found in the model are trapped near the front; m_1 extends almost to the whole water column. Topography causes noticeable changes near the shelf break where the shoreward contours are squeezed toward the area of greater depth by the continental shelf. On the seaward side of the front, perturbation signals become stronger and more surface trapped. The most obvious difference between m_1 and m_2 is that the latter is surface trapped. The second important difference is that m_2 appears slightly offshore compared with the first mode; m_2 is centered around $x = 1.3$, whereas m_1 is centered around $x = 1.0$. The second mode in Fig. 9b is again surface trapped although its vertical extension increases slightly in the case with topography. Moreover, this mode is less affected by the continental shelf because it exists farther offshore.

Mooring data obtained off the Georgia coast (Lee and Atkinson 1983) show that the amplitude of perturbation velocity, δv_a, is about 40 cm s^{-1} or 20% of the maximum velocity of the stream, V_0, and the corresponding amplitude of perturbation temperature, δT_a, is between 2°C and 3°C. We use the following relation derived from (2.5) to estimate the amplitude of temperature perturbation for $\mathcal{P} = 0.20$, which is the ratio of the amplitude of the observed perturbation velocity to the maximum velocity of the Gulf Stream:

$$\delta T_a = -\mathcal{P}\left(\frac{b_a}{v_a}\right)\left(\frac{\rho_0(fL_0V_0/H_0)}{g(\partial\rho/\partial T)_{T_0}}\right), \qquad (4.2)$$

where $\rho_0 = 1025$ kg m^{-3} is the reference density; coefficient of thermal expansion, $(\partial\rho/\partial T)_{T_0}$, is -0.254 kg m^{-3} °C^{-1}; f, L_0, H_0, and V_0 have been given in Table 2; $b_a = (b/h)_{\max}$ and $v_a = (v/h)_{\max}$ are the calculated amplitudes of nondimensional perturbation buoyancy and velocity, respectively. Using the front

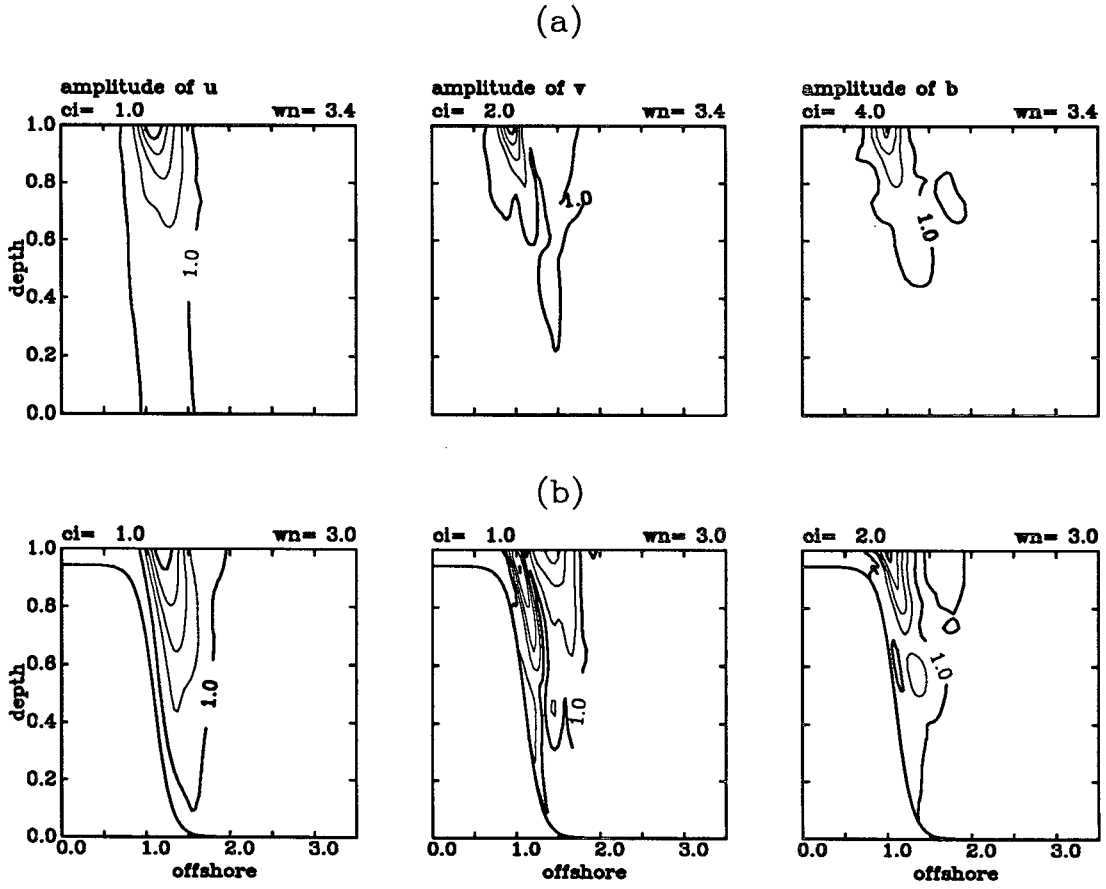

FIG. 8. The amplitude of perturbed velocities and buoyancy of the first unstable mode, m_1: (a) corresponds to front I_0; (b) corresponds to front I_1.

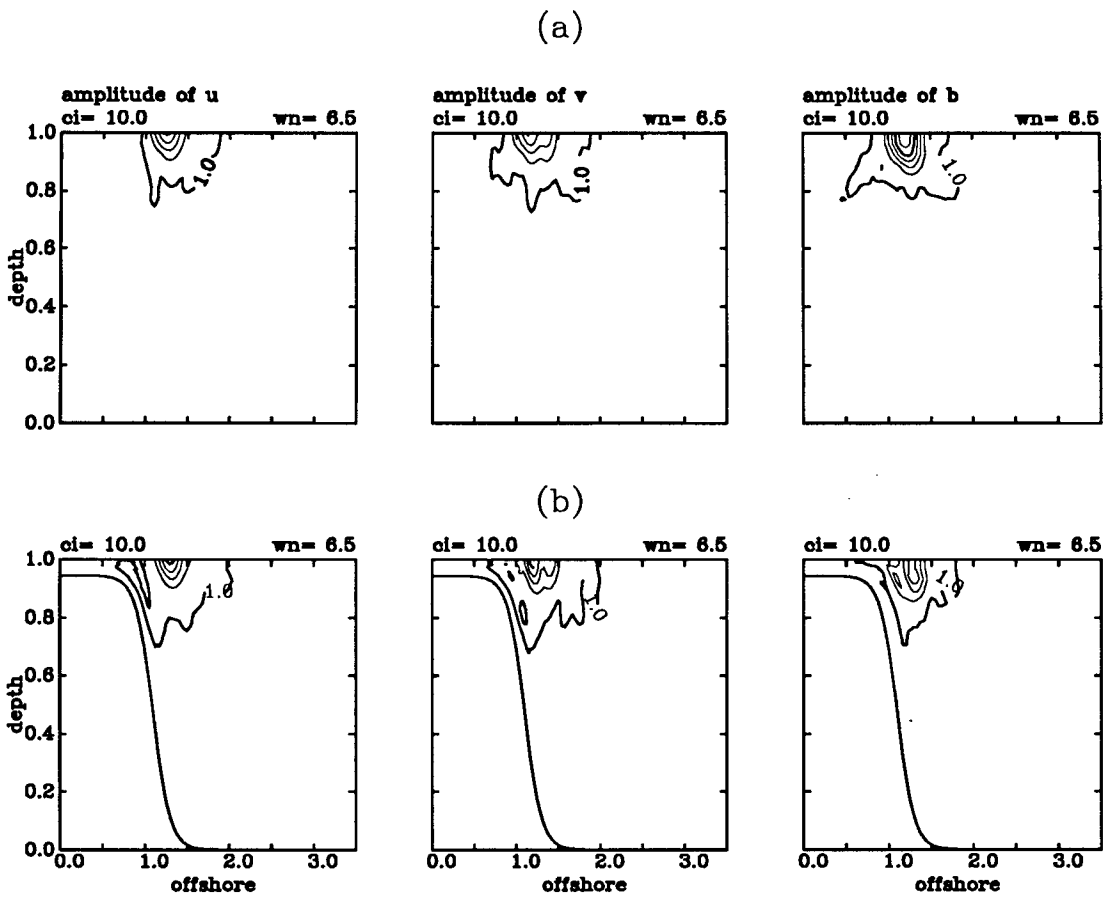

FIG. 9. As in Fig. 8 except for the second mode, m_2.

zone, I_1, to represent the Gulf Stream between Cape Canaveral and the Charleston Bump, the amplitude of the most unstable wave shown in Fig. 8b is similar to the observed; for a 20% variation in perturbation velocity, the amplitude of temperature variation is 2.5°C.

The horizontal sections in Figs. 10 and 11 are total fields constructed according to

$$\mathbf{V} = \frac{\mathcal{P}}{v_a}\left(\frac{u}{h}\right)\mathbf{i} + \left(\frac{\mathcal{P}}{v_a}\frac{v}{h} + \frac{\bar{V}(x,\zeta)}{V_0}\right)\mathbf{j} \qquad (4.3a)$$

$$w = \frac{\mathcal{P}}{v_a}\left(\omega + (\zeta - 1)\frac{\partial h}{\partial x}\frac{u}{h}\right) \qquad (4.3b)$$

$$T = \bar{T}(x,\zeta) - \frac{\mathcal{P}}{v_a}\left(\frac{\rho_0 f L_0 V_0/H_0}{g(\partial\rho/\partial T)_{T_0}}\right)\frac{b}{h}. \qquad (4.3c)$$

They cover one wavelength in the alongfront direction and between $x = 0.5$ and 2.5 in the cross-front direction where the unstable modes occur. Temperature and horizontal velocity plots are located at the surface ($\zeta = 1$), and the vertical velocity plots are located at $\zeta = 7/8$.

The frontal zone, which is originally uniform in the alongfront direction, has been distorted by the three-dimensional unstable waves. The most unstable wave along front I_0, upper panels in Fig. 10, has a cold center along the shoreward side of the front, and the cold water pushes the front offshore and intensifies the thermal gradient across the front. The downstream scale of this cold water is almost four times its own width. The horizontal velocity shows the type of wave motion described by Webster (1961). A cyclonic circulation is associated with the cold water, and an anticyclonic circulation is associated with a weaker warm anomaly on the seaward side of the front, although it is not clear in the plot of total velocity. The center of the cyclonic circulation leads the center of the cold water by one-eighth wavelength. Such a configuration causes energy transfer from the mean potential energy to the eddy potential energy. The vertical velocity shown in the right panels indicates that upwelling (downwelling) appears in the leading (trailing) portion of the cold water. Such a pattern provides a favorable condition for energy transfer from eddy potential energy to eddy kinetic energy.

The basic structures described above remain for the

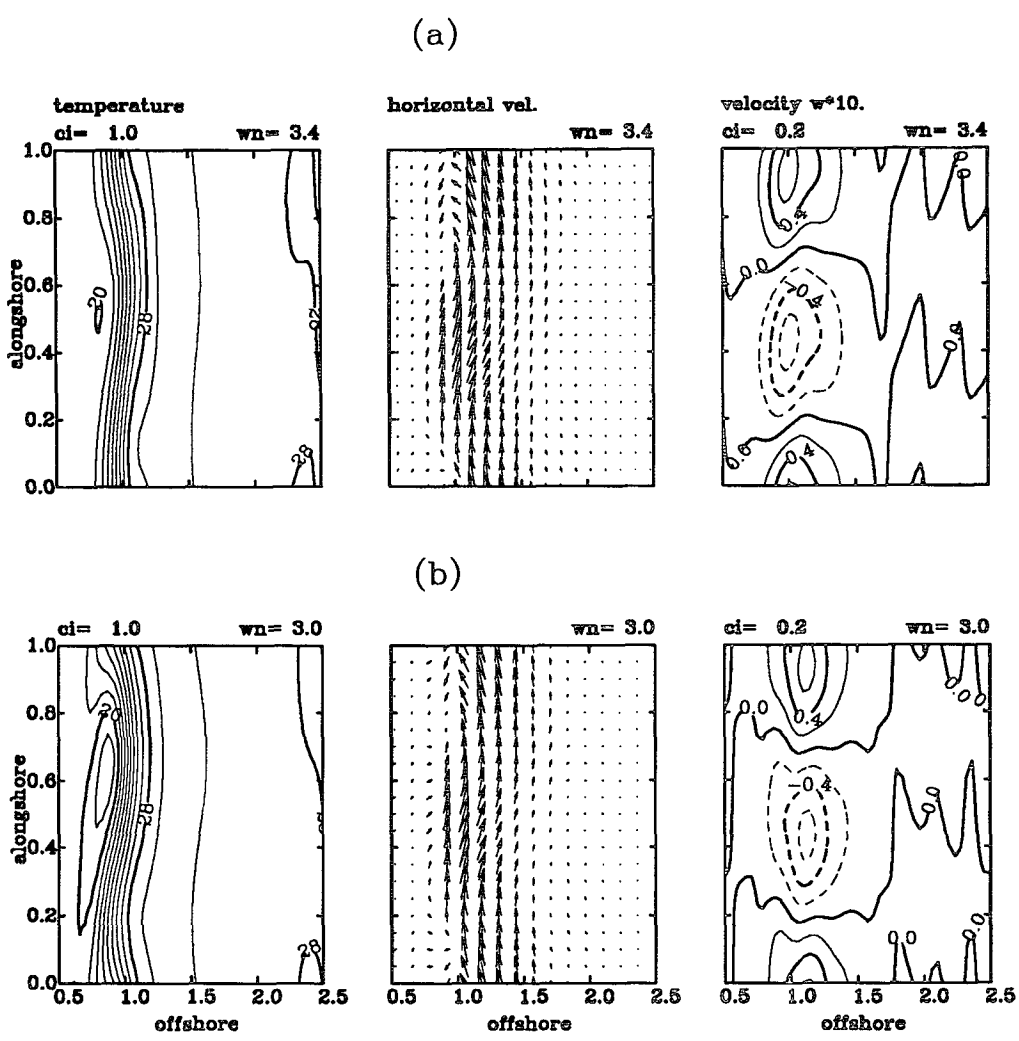

FIG. 10. Superposition of m_1 perturbation and the mean frontal structure at horizontal cross sections. Plots of the temperature and horizontal velocity are at the surface; plots of the vertical velocity are at $\zeta = 7/8$. Dashed contours indicate negative values. Quantities are dimensionless except for the surface temperature: (a) corresponds to front I_0; (b) corresponds to front I_1.

most unstable mode after including the topography (lower panels in Fig. 10). The perturbed temperature has a larger amplitude in the case with the topography if the same amplitude of the perturbed velocity is assumed. Second, the distance between the cold water center and the center of cyclonic circulation and the distance between the cold water center and upwelling center have changed, which affects the correlation between the perturbation buoyancy and perturbation velocities.

The second mode along front I_0 (upper panels in Fig. 11), distorts the front in a different manner. The largest changes of the isotherms occur on the seaward side of the front because this mode exists farther offshore. The mean current is deflected offshore by a cold anomaly, and it is forced toward the shore in the trailing portion of a cold anomaly. The southward flow generated by a cold anomaly is near the axis of the mean current, and it is not strong enough to counteract the effects of the mean current. Thus, no cyclonic circulation is formed. Associated with the center of a warm anomaly, the total velocity shows a double jet with the stronger one on the seaward side. On the other hand, the southward flow generated by a cold anomaly is on the offshore side of the mean current, and it is able to completely counteract the effect of the mean current there. Thus, the total flow becomes a stronger but narrower current on the shoreward side. After adding the topography, there are no qualitative differences in the basic pattern of m_2.

The calculation of energy conversion processes is based on Eqs. (C.7), (C.8), and (C.9) and is displayed in Fig. 12. The Reynolds stress (RS) represents conversion between mean kinetic energy and eddy kinetic

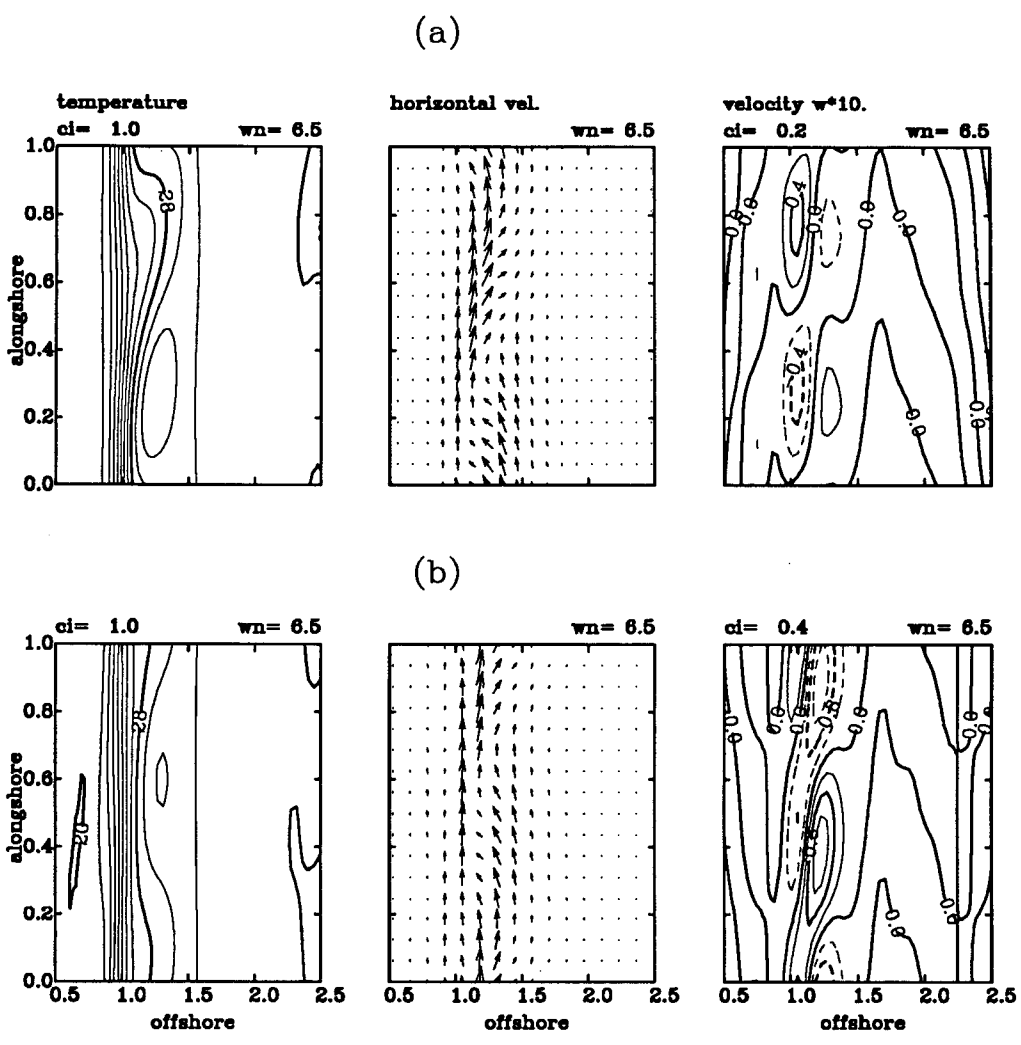

FIG. 11. As in Fig. 10 except for the superposition of m_2 perturbation and the mean frontal structure.

energy; the horizontal heat flux (HHF) represents conversion between mean available potential energy and eddy potential energy, and the vertical heat flux (VHF) represents the conversion between eddy potential energy and eddy kinetic energy. Figure 12 shows where energy conversions occur and their magnitudes. It indicates the sources or sinks of the eddy energies, although the eddy kinetic energy may grow or decay at locations different from those shown in Fig. 12 because of possible contributions from pressure work terms.

As observed (Lee et al. 1981; Hood and Bane 1983), all conversion terms have significant values only within a very narrow region on the shoreward side of the front. Second, they are confined to the top of the water column. The first mode has positive HHF in both the flat bottom case and the case with the topography. However, unlike the observed results, RS values are positive in both cases. Therefore, both barotropic and baroclinic instabilities contribute to the development of meanders. HHF and RS have maxima at the surface, but VHF is zero at the surface because of the rigid-lid approximation. Reynolds stress is hardly affected by the presence of the topography. On the other hand, both HHF and VHF change considerably after including the topography. HHF is reduced in the upper water column, especially near the inner slope where the maximum baroclinicity occurs and where the topographic slopes exceed the slopes of isopycnals at the bottom.

Energy flow diagrams in Fig. 13 are obtained by integrating over the cross section. The quantities are normalized with respect to the horizontal heat flux of each mode in the flat bottom case; therefore, energy conversion processes of each mode are compared between two cases only when the same amplitude is assumed. For the first mode, m_1, the baroclinic conversion, HHF, is about three times the barotropic conversion, RS, and about one-third of the eddy potential energy is transferred to the eddy kinetic energy through VHF. After

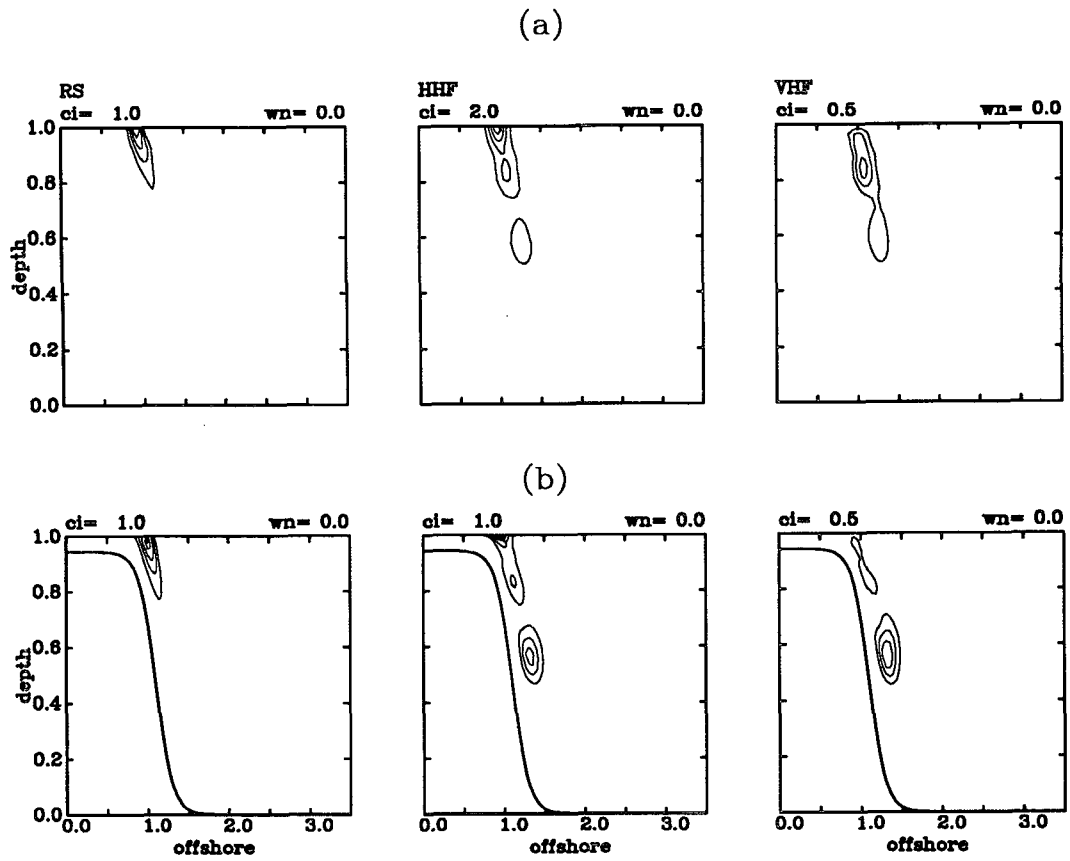

FIG. 12. Energy conversions of the most unstable wave: (a) associated with front I_0, and (b) associated with front I_1.

inclusion of topography, the baroclinic conversion is reduced by almost 40%, so that there is less eddy potential energy converted to the eddy kinetic energy. The bottom slope is effective only in stabilizing baroclinic conversion. In fact, barotropic instability is hardly affected by topography. Therefore, the baroclinic conversion contributes approximately two-thirds of eddy energy for the most unstable wave in the case with the topography.

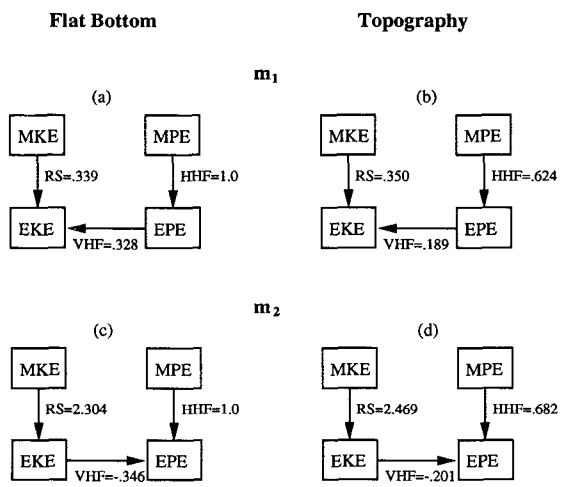

FIG. 13. Energy flow diagrams: (a) and (c) correspond to m_1 and m_2 of front I_0; (b) and (d) correspond to m_1 and m_2 of front I_1.

The energetics of the second mode, m_2, is significantly different from the first mode. Barotropic instability is the dominant mechanism for m_2 and contributes two-thirds of eddy energy in the flat bottom case and three-quarters of eddy energy in the case with the topography. As a result, part of the eddy kinetic energy is converted to eddy potential energy through negative VHF. The conclusion that the bottom slope is effective only in stabilizing baroclinic instability can be drawn for m_2 as well. The baroclinic conversion of m_2 decreases by more than 30% after incorporating the topography. However, barotropic conversion is slightly enhanced.

c. Cross section downstream of the Charleston Bump

After application of the same model to the frontal zones II_0 and II_1, the resultant growth rate and phase speed spectra are given in Fig. 14 and Fig.15. As with cross section I, the growth rate spectra at long waves

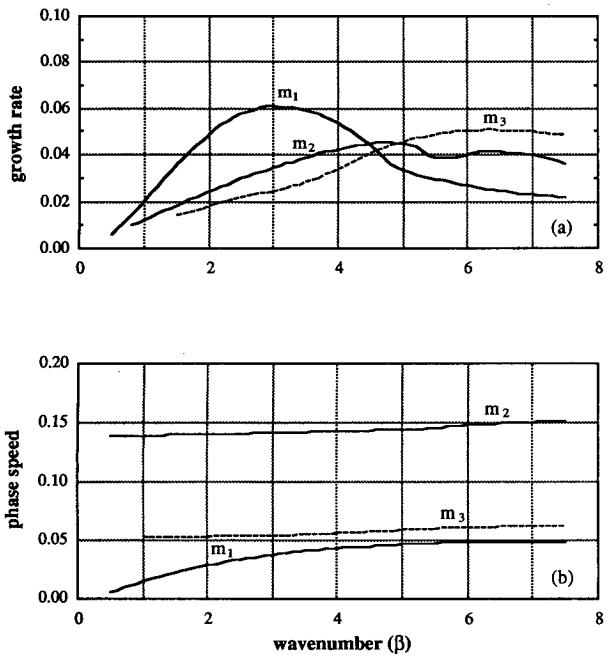

FIG. 14. Growth rate spectra (a) and phase speed spectra (b) of the two most unstable modes growing on front II_0, flat bottom. All quantities are nondimensionalized according to (2.5).

are similar to quasigeostrophic solutions, and there are unstable short waves as well. Moreover, except when the wavenumber is really small, topographic effects also reduce the growth rate, increase phase speeds at all wave numbers, and decrease the wavenumber associated with the most unstable wave. Nevertheless, the growth rate and the phase speed are generally smaller than those in Figs. 6 and 7.

With this new mean condition, the most unstable wave in the flat bottom case occurs at wavenumber 3.0 with a growth rate of 0.062. It is equivalent to a wavelength of 215 km and an *e*-folding time scale of 2.4 days. The most unstable wave has a phase speed of 0.038, which corresponds to a dimensional propagation speed of 26.1 km day^{-1}. It is different from the results of cross section I in that the most unstable wave on the short-wave side belongs to the third mode, m_3. It has the maximum growth rate of 0.051 at wavenumber 6.5. The second mode, m_2, is the second unstable mode both at short waves and long waves. Phase speeds of both m_2 and m_3 increase linearly as wavenumber increases, and m_3 has a phase speed of 0.062 at wavenumber 6.5. The most unstable wave in the case with the topography (Fig. 15) occurs at wavenumber 2.8 with a growth rate of 0.047. It is equivalent to a wavelength of 225 km and an *e*-folding time scale of 3.2 days. This wave moves at a phase speed of 0.052, which corresponds to a propagation speed of 35 km day^{-1}. As in the flat bottom case, the most unstable wave on the short-wave side belongs to m_3. It has a maximum growth rate of 0.041 occurring at wavenumber 6.3. It is equivalent to a dimensional wavelength of 100 km. The phase speed of the m_3 mode is 0.079, which corresponds to a dimensional propagation speed of 53.2 km day^{-1}.

Since m_2 is the less unstable mode compared to m_1 at long-wave lengths and to m_3 at short-wave lengths, its mode structure is not shown. Nevertheless, m_2 has cross-sectional distributions similar to its cross section I counterpart and is trapped near the surface.

Figures 16 and 17 are the structure functions for u, v, and b of m_1 and m_3. Both modes are trapped along the front; m_1 exists within the upper one-third of the water column, which is about the depth of the mean current. In cross section I, the Gulf Stream extends to the bottom, as does the most unstable mode. Thus, the first mode has a vertical scale comparable to the vertical scale of the Gulf Stream. Generally speaking, the perturbation signal on the seaward side is stronger compared to that of cross section I. Changes of m_1 due to the topography are similar to those of cross section I. For the downstream velocity component, the flow branch on the seaward side expands and is enhanced. A third flow branch emerges farther offshore so that this mode has two nodes across the front. In fact, the type of velocity cross section seen in the upper and middle panels of Fig. 16b generates anticyclonic circulations on the seaward side of the front associated with warm anomalies. The upper part of the flow branch on the shoreward side is less affected by the topography compared to cross section I, because the shelf break has a larger depth in cross section II. The lower part is again pushed offshore. The amplitude of

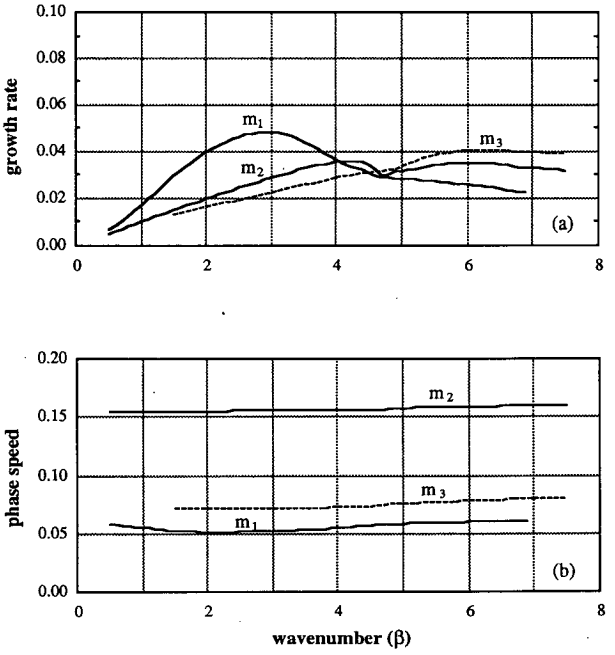

FIG. 15. As in Fig. 14 except for front II_1, with bottom topography.

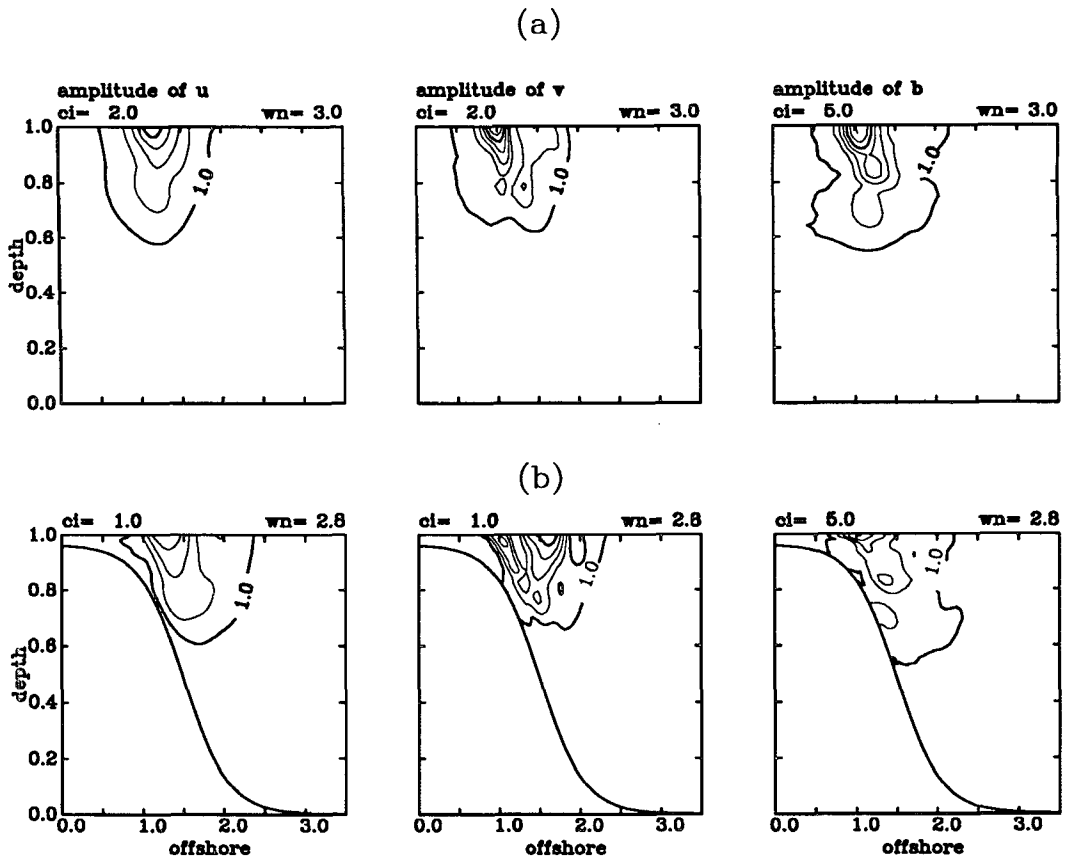

FIG. 16. The amplitude of perturbed velocities and buoyancy of the first unstable mode, m_1: (a) corresponds to front II_0; (b) corresponds to front II_1.

perturbation temperature in Fig. 16b, estimated according to equation (4.2), is 3.0°C if the amplitude of the perturbation velocity is 20% of the maximum velocity of the mean current, and this agrees with the observations off the Carolina coast (Bane et al. 1981). The third mode, m_3, has a vertical scale similar to the first mode. Of the three modes, it is the farthest from the coast. Similar to m_1, m_3 forms two circulations across the front, which are in opposite direction. However, unlike m_1, at the surface m_3 is stronger on the seaward side, and it is wider on the shoreward side and has the maximum below the surface. The structural changes of mode m_3 due to topographic effects are rather small in vertical cross sections.

Figure 18 shows that the m_1 mode for the II_0 and II_1 fronts is similar. Common features include cold anomalies on the shoreward side of the front that push the front offshore so that the cross-front thermal gradient increases. Cyclonic circulations are associated with the cold anomalies on the shoreward side of the front where the main body of the mean current shifts offshore and intensifies. The cyclonic circulation patterns are not symmetric in the alongfront direction. The large transverse velocity occurs in the leading portion of the cyclonic circulation. Upwelling always leads the cold anomaly. The strength and the cross-front scale of the upwelling (downwelling) associated with cold (warm) temperature anomaly patterns increase after including the topography. In comparison with their cross section I counterparts (Fig. 10), the cold anomaly becomes stronger, and there is a warm tongue extending southward on the western side of the cold anomaly in the case with the topography. Although this warm tongue is different from the observed warm filament, it at least shows the possible development of an interleaving structure when the amplitude of the perturbation temperature is large enough. The anticyclonic circulation on the seaward side of the front is very clear, especially in the case with the topography.

The m_3 mode in Fig. 19 has a more complicated cross-front pattern. Anomaly signatures can be seen on both sides of the front. They are stronger on the seaward side in the flat bottom case. For this mode, the cold center leads the cyclonic circulation on the offshore side of the front but it trails the upwelling. After including the topography, perturbation signals on the shoreward side of the front become stronger than those on the seaward side. The relative pattern

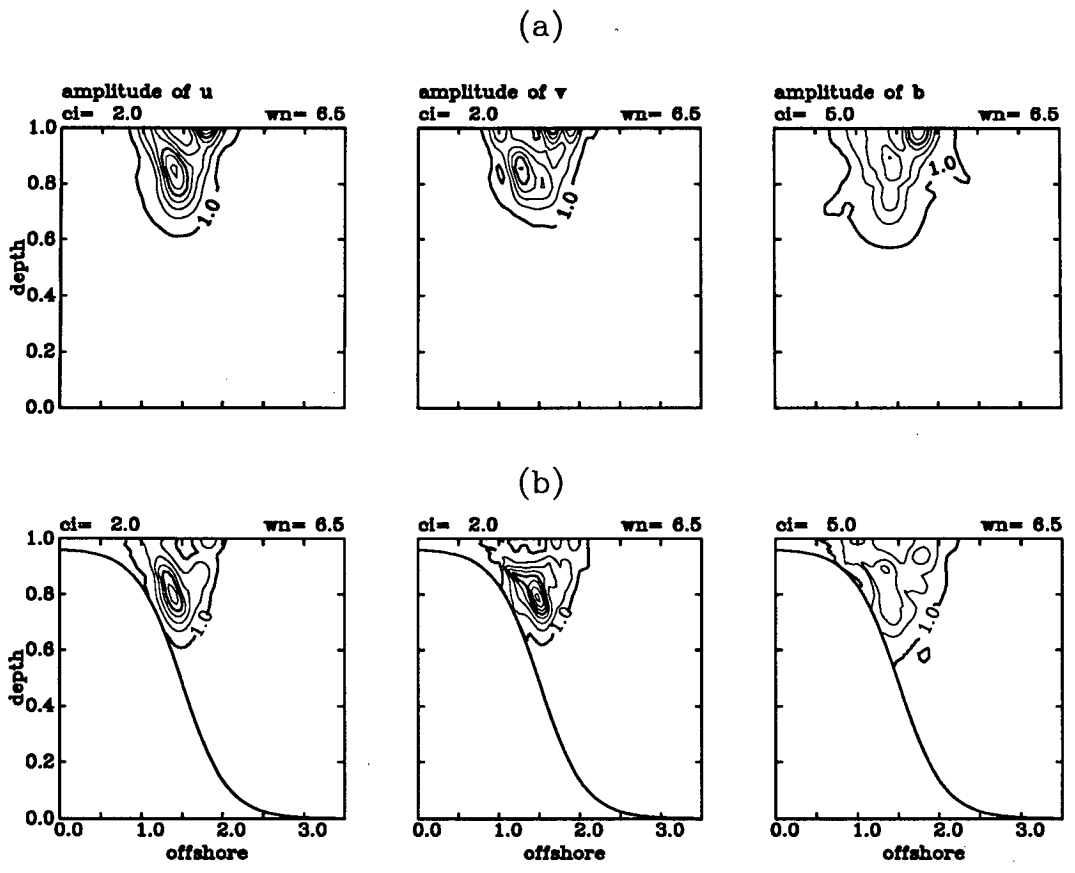

FIG. 17. As in Fig. 16 except for the third mode, m_3.

among the cold center, the cyclonic circulation, and the upwelling remains.

Energy conversions of the m_1 mode (Fig. 20) have significant values only within a narrow region on the shoreward side of the mean current, although they have larger scales in the cross-front direction compared with those of cross section I because cross section II is wider. HHF and RS are positive in both cases so that both barotropic and baroclinic instabilities operate simultaneously for this unstable mode. Generally speaking, changes due to the topography are similar for both cross sections. HHF and VHF have considerable changes when the topography is added. Reynolds stress is hardly affected, whereas both HHF and VHF are reduced, especially near the shelf break.

Energy flow diagrams in Fig. 21 again show a noticeable decrease in baroclinic conversion after inclusion of topography. In the flat bottom case, the baroclinic conversion of m_1 is about seven times the barotropic conversion, and there is a considerable amount of eddy potential energy converted to the eddy kinetic energy. The baroclinic conversion is reduced by more than 20%, and the barotropic conversion increases slightly by adding the topography. Therefore, baroclinic instability accounts for approximately 80% of eddy energy for the most unstable wave in the case with the topography. The third mode, m_3, is different from both m_1 and m_2 in terms of its energetics. It generates countergradient momentum flux so that RS is negative. Baroclinic instability is the only mechanism operating with m_3. Nevertheless, it is still true that the topography reduces the baroclinic instability.

5. Discussion

a. Stabilizing effects of the bottom topography on baroclinic instability

Four individual frontal zones have been studied. Growth rates of the most unstable wave associated with these four frontal zones are summarized in Table 3. It is clear that the topography is a stabilizing factor for baroclinic instability. Barotropic instability is enhanced slightly according to the present study.

HHF cross-sectional distributions in Fig. 12 and Fig. 20 show that the baroclinic energy conversion is most reduced near the inner slope where the topographic slopes exceed the isopycnic slopes at the bottom. The stabilizing effect of the bottom slope on baroclinic instability can be explained as follows: for baroclinic waves to draw energy from the mean available potential

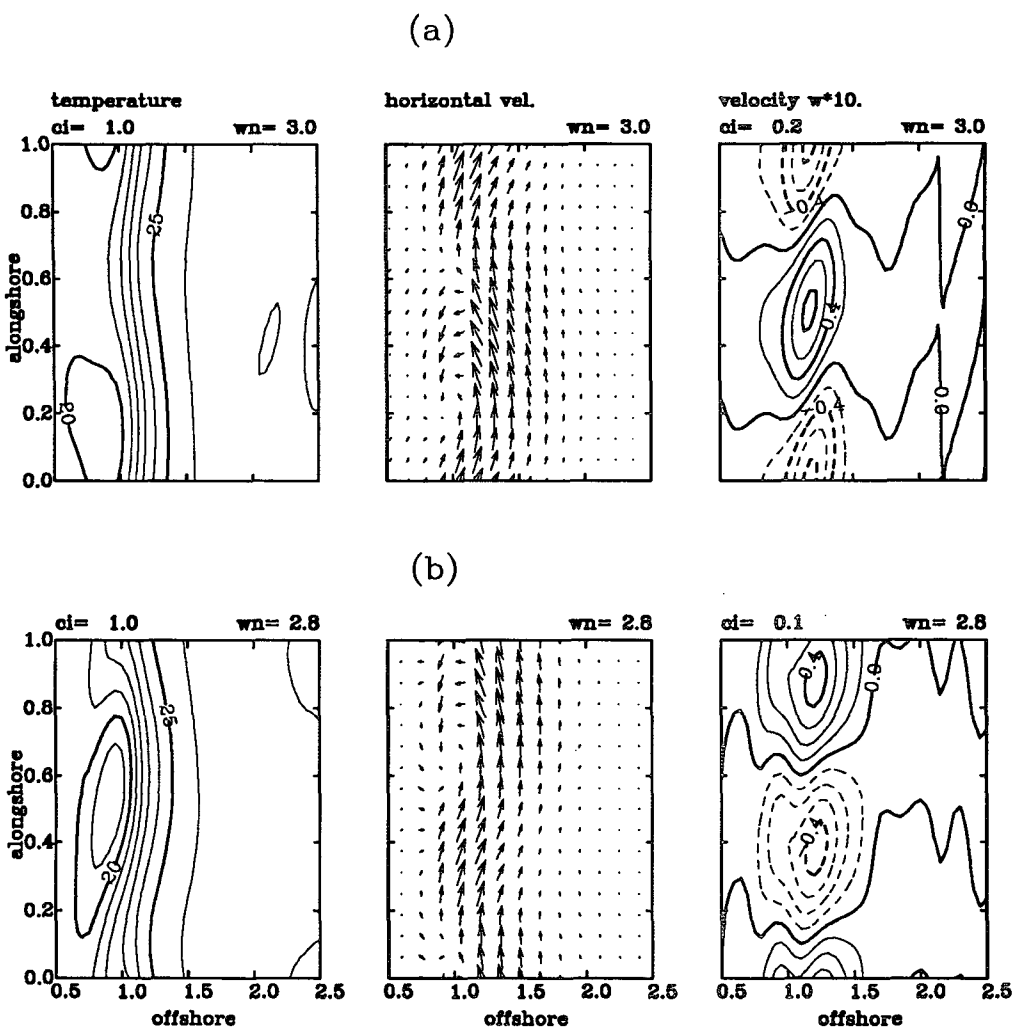

FIG. 18. Superposition of m_1 perturbation and the mean frontal structure at horizontal cross sections. Plots of the temperature and horizontal velocity are at the surface; plots of the vertical velocity are at $\zeta = 7/8$. Dashed contours indicate negative values. Quantities are dimensionless except for the surface temperature: (a) corresponds to front II_0; (b) corresponds to front II_1.

energy, the orientation of the particle paths is between the horizontal and the isopycnals. Since motions are constrained along the bottom topography, cold water is forced upward in the region where the topographic slopes are larger than the slopes of isopycnals. Thus, the loss of the mean potential energy due to baroclinic waves is partly balanced by the increase of the mean potential energy due to upwelling of cold water near the bottom. Therefore, bottom slope is effective in stabilizing the deeper portion of the water column in such regions.

Despite the stabilizing effect of the continental slope, the Gulf Stream is indeed unstable, as evidenced in Table 3. The question is whether perturbations are able to grow into large meanders with the calculated growth rate. One important issue, ignored thus far, is that the SAB has a limited length. One should estimate the amplification within the time duration that meanders actually spend in the SAB. Gaster (1962) has shown that if the growth rate is small compared to the frequency of an unstable mode as for Gulf Stream meanders, the frequency for a disturbance growing with respect to time is the same as that of a spatially growing wave having the same wavenumber. Spatial growth is related to the time growth by the group speed. Based on his concept of quantitatively relating the spatial growth to the temporal growth of unstable waves, we define a total amplification factor as follows:

$$\mathcal{T} = e^{-\sigma_i(L_y/C_{ph})}, \tag{5.1}$$

where $-\sigma_i$ and C_{ph} are the dimensional growth rate and phase speed given in Table 3; L_y is the length of the SAB, which is chosen to be 300 km for both parts of the SAB upstream and downstream of the Charleston

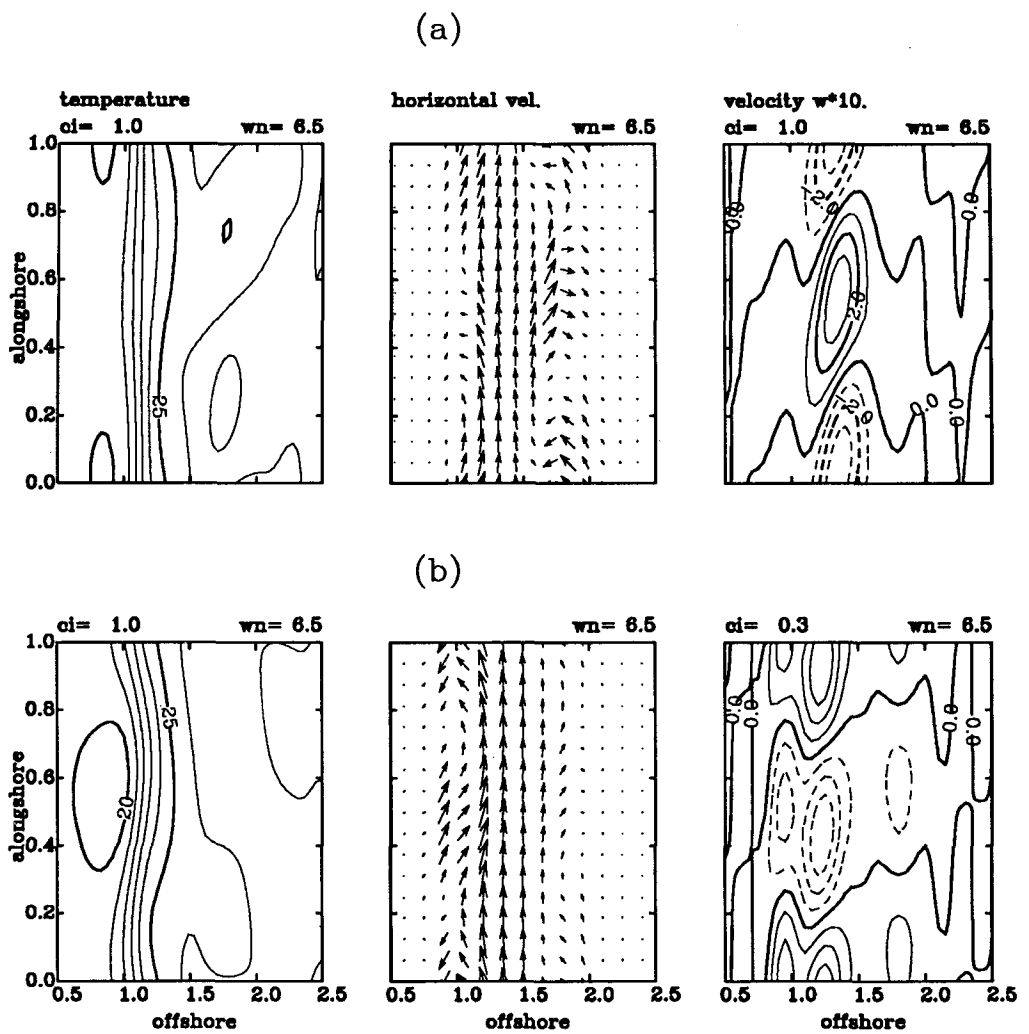

FIG. 19. As in Fig. 18 except for the superposition of m_3 perturbation and the mean frontal structure.

Bump. The estimated total amplification factors of each frontal zone are given in the last column of Table 3. Though the reduction in growth rate is no more than 40%, the total amplification factor reduces considerably after the topography is incorporated due to the combined effects of the reduction in growth rate and the increase in phase speed. Therefore, models with a flat bottom, such as that by Oey (1988), are able to produce finite amplitude meanders, but it is less likely that random perturbations would grow into substantial meanders in the SAB because of the stabilizing effects of the continental slope.

b. Mechanism of unstable short waves

The full hydrostatic primitive equations yield two distinct and well-separated length scales of baroclinic instability (Stone 1970; Moore and Peltier 1987; Nakamura 1988). The first scale is associated with the Charney–Eady mode of baroclinic instability, and the second scale is defined by a new mode of baroclinic instability with a shorter wavelength approximately equal to the Rossby radius of deformation.

Nakamura (1988) showed that unstable short waves emerge at wavenumbers where inertial critical levels appear inside the domain. This is also the point where the Eady's neutral mode and the neutral inertial–gravity mode coalesce. Therefore, the difference between unstable long waves and unstable short waves is that the former is produced by a coupling between two boundary modes and the latter is produced by a coupling between one boundary mode and inertial–gravity modes. The main energy source of unstable short waves is still baroclinic conversion of potential energy, which takes place between one of the boundaries and the critical level. The unstable short-wave solution of Stone (1970) and Nakamura (1988) may not be directly relevant to the strong cyclogeneses in the atmosphere since the growth rate is far smaller than that of the Eady

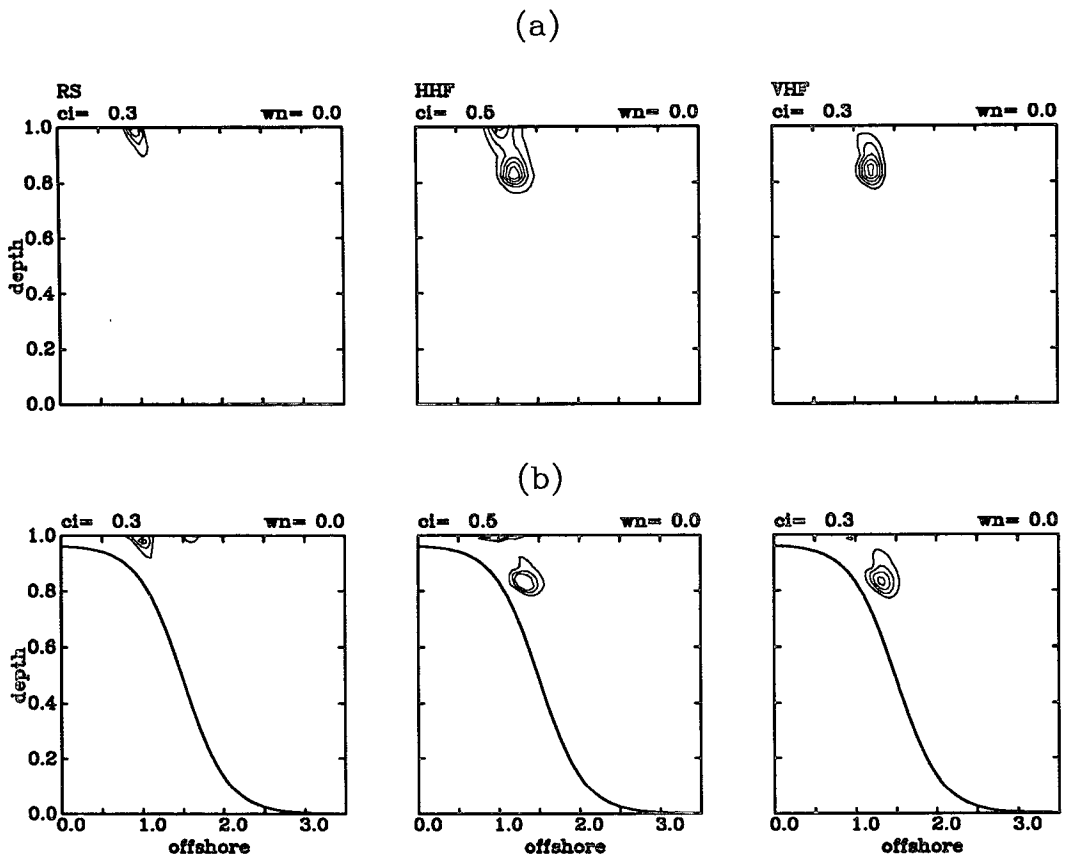

FIG. 20. Energy conversions of the most unstable wave (a) associated with front II_0 and (b) associated with front II_1.

mode. However, short waves generally become more unstable as the cross-front wavenumber increases (Stone 1970).

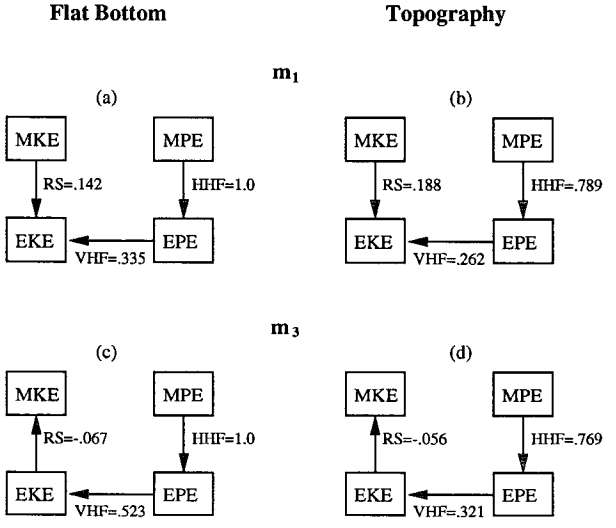

FIG. 21. Energy flow diagrams: (a) and (c) correspond to m_1 and m_3 of front II_0; (b) and (d) correspond to m_1 and m_3 of front II_1.

Moreover, the cross-front gradient of the mean potential vorticity also generates unstable, short-wave branches (McIntyre 1970). The critical layer theory shows that there is a tendency for baroclinic waves to generate a countergradient momentum flux. Therefore, the growth rate of Charney–Eady mode is reduced in both Moore and Peltier (1987) and in the present study after taking into account the cross-front gradients. Both long-wave branches and short-wave branches have comparable growth rates. Numerical experiments indicate that the short-wave instability becomes stronger when the front is narrower than the radius of deformation.

TABLE 3. Characteristics of the most unstable wave and its energy conversions for the four frontal zones; λ is the wavelength. Given in the last column is the total amplification factor $\mathcal{T}$.

Front	$-\sigma_i/f$	C_{ph} (km d^{-1})	λ (km)	HHF	VHF	RS	$\mathcal{T}$
I_0	0.088	30.8	185	1.000	.328	.339	217.9
I_1	0.055	39.3	215	.624	.189	.350	14.0
II_0	0.062	26.1	215	1.000	.335	.142	105.0
II_1	0.048	35.0	225	.789	.262	.188	15.9

Both mechanisms can be found in the unstable short waves of the present study. The second mode, m_2, is similar to the cyclone-scale mode in Moore and Peltier (1987); they are boundary trapped, and the vertical scale is determined by the critical level, as explained by Nakamura (1988). However, the horizontal velocity gradient favors barotropic instability. Thus, the resultant unstable modes have growth rates comparable to unstable long waves, but barotropic instability is dominant. On the other hand, m_3 is the type of unstable short wave discussed by McIntyre (1970). It has the same vertical scale as the unstable long waves and yet has a countergradient momentum, that is, a negative RS.

Both m_2 and m_3 structure functions are stronger on the seaward side of the front. It is likely to associate them with wavy patterns seen along the Sargasso Sea side of the Gulf Stream front (Fig. 1). Since those frontal structures are not well documented in the literature, it is inappropriate to make any further comparisons.

6. Conclusions

The most important influence of the continental slope on the Gulf Stream is to reduce baroclinic instability associated with the front. Second, the wavelength of the most unstable wave increases, the corresponding phase speed increases, and the variation of the phase speed with the alongfront wavenumber is reduced so that each unstable mode is less dispersive in the case with the topography.

Table 3 lists characteristics of the most unstable wave. If fronts I_1 and II_1 represent the averaged Gulf Stream front upstream and downstream of the Charleston Bump, the increase of wavelength from 215 to 225 km and the decrease of phase speed from 39.3 to 33.7 km day^{-1} agree with observed meander characteristics and their changes along the SAB (Lee et al. 1981; Bane 1983). The present study suggests that at least part of the changes of the meander characteristics along the SAB are due to the changes of properties of the most unstable wave associated with the different mean conditions of the Gulf Stream at various locations along the SAB.

Generally speaking, this linear and inviscid model successfully explains the preferred scales of Gulf Stream frontal meanders not only in terms of wavelength and phase speed but also in terms of mode structures. First of all, the most unstable wave appears on the cyclonic shear side of the front. For this mode, a cyclonic circulation and upwelling lead a cold anomaly, and this is the basic structure of the cold water dome observed on the shoreward side of the Gulf Stream front. Second, mode structures associated with the most unstable wave give a good estimate of the temperature change relative to observed changes of the perturbation velocity. For instance, if the maximum velocity of the unstable wave is 20% of the maximum velocity of the Gulf Stream, the estimated amplitude of temperature variation is 2.5°C for cross section I and 3.0°C for cross section II.

However, the shape of the cold water and the warm filament is different between the numerical results and the observed meanders. First of all, the observed cold water has comparable scales in the alongfront and in the cross-front directions, whereas in the model the cold water has an alongfront scale about four to five times its scale in the cross-front direction. Second, although there is an indication of a warm tongue formation when an anomaly is strong enough, as shown in Fig. 18, the alongfront scale of this warm tongue can hardly compare with the observed scale of warm filaments. Nevertheless, the existence of such warm tongues at least provides the possibility of being developed into features similar to those observed due to nonlinear evolution, as explained by Stern (1985). If the warm filaments can extend southward substantially, the cold water found in the linear solution may become less elongated and may result in more realistic meander patterns.

Acknowledgments. We thank Drs. K. Moore and W. Peltier for providing their spectral model, and Drs. K. Bryan, I. Held, and I. Orlanski for their valuable comments. The research was supported by the Institute for Naval Oceanography under Contract INO-S8751 and by NOAA's Geophysical Fluid Dynamics Laboratory.

APPENDIX A

Residual Equations and Definitions

a. The residual equations

$$R_1 = \sum_{\nu=0}^{N} \left\{ (\sigma + \mathrm{Ro}\beta V) u_\nu E_\nu - v_\nu E_\nu + h \frac{\partial p_\nu}{\partial x} E_\nu - (\zeta - 1) \frac{\partial h}{\partial x} b_\nu F_\nu \right\} \quad \text{(A.1a)}$$

$$R_2 = \sum_{\nu=0}^{N} \left\{ \sigma + \mathrm{Ro}\beta V) v_\nu E_\nu - (1 + \mathrm{Ro} V_x) u_\nu E_\nu - \mathrm{Ro} V_\zeta \omega_\nu F_\nu + \beta h p_\nu E_\nu \right\} \quad \text{(A.1b)}$$

$$R_3 = \sum_{\nu=0}^{N} \{ b_\nu F_\nu + \nu\pi p_\nu F_\nu \} \quad \text{(A.1c)}$$

$$R_4 = \sum_{\nu=0}^{N} \left\{ \frac{\partial u_\nu}{\partial x} E_\nu - \beta v_\nu E_\nu + \nu\pi \omega_\nu E_\nu \right\} \quad \text{(A.1d)}$$

$$R_5 = \sum_{\nu=0}^{N} \{ (\sigma + \mathrm{Ro}\beta V) b_\nu F_\nu - S B_x u_\nu E_\nu - S B_\zeta \omega_\nu F_\nu \}. \quad \text{(A.1e)}$$

Equations, (A.1a), (A.1b), and (A.1e) are prognostic equations; (A.1c) and (A.1d) are diagnostic equations.

b. Definition of the matrix P, $J^p_{\gamma 0\lambda\nu}$ and $M^q_{\kappa\mu\lambda\nu}$

$$P_{\gamma\lambda} = \frac{\gamma\pi}{L}\frac{\lambda\pi}{L}[\psi_\gamma h\psi_\lambda] + \frac{\beta^2}{(1+\delta_{\gamma 0})}[\phi_\gamma h\phi_\gamma];$$

$$P^{-1}_{\kappa\gamma}P_{\gamma\lambda} = \delta_{\kappa\lambda} \quad \text{(A.2)}$$

$$J^1_{\gamma 0\lambda 0} = -\left(\frac{\gamma^2\pi^2}{L^2} + \frac{\beta^2}{(1+\delta_{\gamma 0})}\right)\frac{4\lambda \bmod_2(\gamma-\lambda)}{\beta(\gamma^2-\lambda^2)\pi} + \frac{\mathrm{Ro}\beta}{2}\left\{\frac{\gamma\pi}{L}[\psi_\gamma\langle E_0 V E_0\rangle\psi_\lambda] + \left([\phi_\gamma\langle E_0 V_x E_0\rangle\psi_\lambda] - \frac{\lambda\pi}{L}[\phi_\gamma\langle E_0 V E_0\rangle\phi_\lambda]\right)\Big/(1+\delta_{\gamma 0})\right\} \quad \text{(A.3a)}$$

$$J^2_{\gamma 0\lambda\nu} = \frac{\mathrm{Ro}\beta}{2}\left\{\frac{\gamma\pi}{L}[\psi_\gamma\langle E_0 V E_\nu\rangle\psi_\lambda\rangle] + \left([\phi_\gamma\langle E_0 V_x E_\nu\rangle\psi_\lambda] - \frac{1}{\nu\pi}\frac{\lambda\pi}{L} \times [\phi_\gamma\langle E_0 V_\zeta F_\nu\rangle\phi_\lambda]\right)\Big/(1+\delta_{\gamma 0})\right\} \quad \text{(A.3b)}$$

$$J^3_{\gamma 0\lambda\nu} = -\frac{\mathrm{Ro}\beta^2}{2(1+\delta_{\gamma 0})}\left([\phi_\gamma\langle E_0 V E_\nu\rangle\phi_\lambda] - \frac{1}{\nu\pi}[\phi_\gamma\langle E_0 V_\zeta F_\nu\rangle\phi_\lambda]\right) \quad \text{(A.3c)}$$

$$J^4_{\gamma 0\lambda\nu} = \frac{1}{\nu\pi}\frac{\gamma\pi}{L}[\psi_\gamma h_x\phi_\lambda] \quad \text{(A.3d)}$$

$$M^1_{\kappa\mu\lambda\nu} = -\frac{\mathrm{Ro}\beta}{(1+\delta_{\mu 0})}[\psi_k\langle E_\mu V E_\nu\rangle\psi_\lambda] + I^1_{\kappa 0\lambda\nu}\delta_{\mu 0} \quad \text{(A.4)}$$

$$M^2_{\kappa\mu\lambda\nu} = \delta_{\mu\nu(\mu\geqslant 1)}\frac{4\kappa \bmod_2(\kappa-\lambda)}{(\kappa^2-\lambda^2)\pi} + I^2_{\kappa 0\lambda\nu}\delta_{\mu 0} \quad \text{(A.5)}$$

$$M^3_{\kappa\mu\lambda\nu} = \frac{\langle E_\mu(\zeta-1)F_\nu\rangle}{(1+\delta_{\mu 0})}[\psi_\kappa h_x\phi_\lambda] - \frac{\delta_{\mu\nu(\mu\geqslant 1)}}{\mu\pi}\frac{\lambda\pi}{L}[\psi_\kappa h\psi_\lambda] + I^3_{\kappa 0\lambda\nu}\delta_{\mu 0} \quad \text{(A.6)}$$

$$M^4_{\kappa\mu\lambda\nu} = \frac{\mathrm{Ro}}{(1+\delta_{\kappa 0})}\{[\phi_\kappa\langle E_\mu V_x E_\nu\rangle\psi_\lambda] + I^4_{\kappa\mu\lambda\nu}\} - \frac{\delta_{\mu\nu}4\lambda \bmod_2(\kappa-\lambda)}{(1+\delta_{\kappa 0})(\kappa^2-\lambda^2)\pi} \quad \text{(A.7)}$$

$$M^5_{\kappa\mu\lambda\nu} = -\frac{\mathrm{Ro}\beta}{(1+\delta_{\kappa 0})}\left\{[\phi_\kappa\langle E_\mu V E_\nu\rangle\phi_\lambda] - \frac{1}{\nu\pi}[\phi_\kappa\langle E_\mu V_\zeta F_\nu\rangle\phi_\lambda]\right\} \quad \text{(A.8)}$$

$$M^6_{\kappa\mu\lambda\nu} = \frac{\delta_{\mu\nu}}{\mu\pi}\frac{\beta}{(1+\delta_{\kappa 0})}[\phi_\kappa h\phi_\lambda] \quad \text{(A.9)}$$

$$M^7_{\kappa\mu\lambda\nu} = \frac{S}{(1+\delta_{\kappa 0})}\{C^{-1}_{\mu\gamma}[\phi_\kappa\langle H_\gamma B_x E_0\rangle\psi_\lambda] - I^7_{\kappa\mu\lambda\nu}\} \quad \text{(A.10)}$$

$$M^8_{\kappa\mu\lambda\nu} = \frac{S\beta}{(1+\delta_{\kappa 0})}\frac{1}{\nu\pi}C^{-1}_{\mu\gamma}[\phi_\kappa\langle H_\gamma B_\zeta E_\nu\rangle\phi_\lambda] \quad \text{(A.11)}$$

$$M^9_{\kappa\mu\lambda\nu} = -\frac{\mathrm{Ro}\beta}{(1+\delta_{\kappa 0})}C^{-1}_{\mu\gamma}[\phi_\kappa\langle H_\gamma V F_\nu\rangle\phi_\lambda] \quad \text{(A.12)}$$

$$I^1_{\kappa 0\lambda\nu} = \begin{cases} \dfrac{4\kappa \bmod_2(\kappa-\lambda)}{(\kappa^2-\lambda^2)\pi}\left(\dfrac{1}{\beta}\dfrac{\lambda\pi}{L}\right) + \dfrac{s\pi}{L}[\psi_\kappa h\psi_s]P^{-1}_{s\gamma}J^1_{\gamma 0\lambda 0}, & \nu = 0 \\ \dfrac{s\pi}{L}[\psi_\kappa h\psi_s]P^{-1}_{s\gamma}J^2_{\gamma 0\lambda\nu}, & \nu \geqslant 1 \end{cases} \quad \text{(A.13)}$$

$$I^2_{\kappa 0\lambda\nu} = \frac{s\pi}{L}[\psi_\kappa h\psi_s]P^{-1}_{s\gamma}J^3_{\gamma 0\lambda\nu}) \quad \text{(A.14)}$$

$$I^3_{\kappa 0\lambda\nu} = \frac{s\pi}{L}[\psi_\kappa h\psi_s]P^{-1}_{s\gamma}J^4_{\gamma 0\lambda\nu} \quad \text{(A.15)}$$

$$I^4_{\kappa\mu\lambda\nu} = \begin{cases} -\dfrac{\lambda\pi}{L}[\phi_\kappa\langle E_\mu V E_0\rangle\phi_\lambda], & \nu = 0 \\ -\dfrac{1}{\nu\pi}\dfrac{\lambda\pi}{L}[\phi_\kappa\langle E_\mu V_\zeta F_\nu\rangle\phi_\lambda], & \nu \geqslant 1 \end{cases} \quad \text{(A.16)}$$

$$I^7_{\kappa\mu\lambda\nu} = \begin{cases} 0, & \nu = 0 \\ \dfrac{1}{\nu\pi}\dfrac{\lambda\pi}{L}C^{-1}_{\mu\gamma}[\phi_\kappa\langle H_\gamma B_\zeta F_\nu\rangle\phi_\lambda], & \nu \geqslant 1. \end{cases} \quad \text{(A.17)}$$

APPENDIX B

Mapping and Definition of Matrix E

Given the triangular truncation scheme ($\mu = 1, 2, \cdots, N$, $\kappa = 1, 2, \cdots N-\mu$), we define

$$i_u(\kappa,\mu) = \mu N - \mu(\mu-1)/2 + \kappa \quad \text{for} \quad 0 \leqslant \mu \leqslant N; \quad 1 \leqslant \kappa \leqslant N-\mu \quad \text{(B.1)}$$

$$i_{vb}(\kappa,\mu) = (N+1)(\mu-1) - \mu(\mu-1)/2 + \kappa + 1 \quad \text{for} \quad 1 \leqslant \mu \leqslant N; \quad 0 \leqslant \kappa \leqslant N-\mu. \quad \text{(B.2)}$$

Equation (B.1) is used because the expansion of $\tilde{u}$ does not include $\kappa = 0$, while (B.2) is needed because the expansion of $\tilde{b}$ does not include $\mu = 0$ and v_0 does not form a prognostic equation due to (2.15a). The total number of elements in **E** will be

$$NE = NPU + NPV + NPB \quad \text{and}$$
$$NPU = NPV = NPB = (N+1)N/2. \quad \text{(B.3)}$$

The one-dimensional vector **V** is defined as

$$\begin{aligned}\mathbf{V}_j &= u_{\kappa\mu} \quad \text{for} \quad j = i_u(\kappa, \mu)\\ &= v_{\kappa\mu} \quad \text{for} \quad j = NPU + i_{vb}(\kappa, \mu)\\ &= b_{\kappa\mu} \quad \text{for} \quad j = NPU + NPV + i_{vb}(\kappa; \mu). \quad \text{(B.4)}\end{aligned}$$

The matrix **E** is defined as follows:

$$\begin{aligned}E_{ij} &= M^1_{\kappa\mu\lambda\nu} \quad \text{for} \quad i = i_u(\kappa, \mu), j = i_u(\lambda, \nu)\\ &= M^2_{\kappa\mu\lambda\nu} \quad \text{for} \quad i = i_u(\kappa, \mu), j = NPU + i_{vb}(\lambda, \nu)\\ &= M^3_{\kappa\mu\lambda\nu} \quad \text{for}\\ &\qquad i = i_u(\kappa, \mu), j = NPU + NPV + i_{vb}(\lambda, \nu)\\ &= M^4_{\kappa\mu\lambda\nu} \quad \text{for} \quad i = NPU + i_{vb}(\kappa, \mu), j = i_u(\lambda, \nu)\\ &= M^5_{\kappa\mu\lambda\nu} \quad \text{for}\\ &\qquad i = NPU + i_{vb}(\kappa, \mu), j = NPU + i_{vb}(\lambda, \nu)\\ &= M^6_{\kappa\mu\lambda\nu} \quad \text{for} \quad i = NPU + i_{vb}(\kappa, \mu),\\ &\qquad j = NPU + NPV + i_{vb}(\lambda, \nu)\\ &= M^7_{\kappa\mu\lambda\nu} \quad \text{for}\\ &\qquad i = NPU + NPV + i_{vb}(\kappa, \mu), j = i_u(\lambda, \nu)\\ &= M^8_{\kappa\mu\lambda\nu} \quad \text{for} \quad i = NPU + NPV + i_{vb}(\kappa, \mu),\\ &\qquad j = NPU + i_{vb}(\lambda, \nu)\\ &= M^9_{\kappa\mu\lambda\nu} \quad \text{for} \quad i = NPU + NPV + i_{vb}(\kappa, \mu),\\ &\qquad j = NPU + NPV + i_{vb}(\lambda, \nu). \quad \text{(B.5)}\end{aligned}$$

APPENDIX C

Mode Structures and Energetics

a. *Transformation from spectral space to physical space*

Eigenvectors obtained after solving (2.18) are in spectral space. They are transformed to the physical space according to

$$\tilde{u}(x, \zeta) = \sum_{\mu=0}^{N} \sum_{\kappa=1}^{N-\mu} \mathbf{X}(i_u(\kappa, \mu)) \cos(\mu\pi\zeta) \sin\left(\frac{\kappa\pi x}{L}\right) \quad \text{(C.1)}$$

$$\tilde{v}(x, \zeta) = \left\{ \sum_{\kappa=1}^{N} \frac{1}{\beta} \frac{\kappa\pi}{L} \mathbf{X}(i_u(\kappa, 0)) + \sum_{\mu=1}^{N} \sum_{\kappa=0}^{N-\mu} \mathbf{X}(NPU + i_{vb}(\kappa, \mu)) \cos(\mu\pi\zeta) \right\} \cos\left(\frac{\kappa\pi x}{L}\right) \quad \text{(C.2)}$$

$$\tilde{b}(x, \zeta) = \sum_{\mu=1}^{N} \sum_{\kappa=0}^{N-\mu} \mathbf{X}(NPU + NPV + i_{vb}(\kappa, \mu)) \times \sin(\mu\pi\zeta) \cos\left(\frac{\kappa\pi x}{L}\right). \quad \text{(C.3)}$$

Here, i_u, i_{vb}, NPU, and NPV are provided by (B.1), (B.2), and (B.3) in appendix B. Therefore, according to (2.6),

$$u = \tilde{u}_a(x, \zeta) \cos(\beta y + \sigma_r t + \phi_u) \cdot e^{-\sigma_i t} \quad \text{(C.4a)}$$
$$v = -\tilde{v}_a(x, \zeta) \sin(\beta y + \sigma_r t + \phi_v) \cdot e^{-\sigma_i t} \quad \text{(C.4b)}$$
$$b = -\tilde{b}_z(x, \zeta) \sin(\beta y + \sigma_r t + \phi_b) \cdot e^{-\sigma_i t}, \quad \text{(C.4c)}$$

where the amplitude and the phase are defined as follows:

$$\tilde{g}_a(x, \zeta) = (\tilde{g}_r^2 + \tilde{g}_i^2)^{1/2} \quad \text{(C.5a)}$$
$$\phi_g = \arctan(\tilde{g}_i/\tilde{g}_r). \quad \text{(C.5b)}$$

Here, g represents either $\tilde{u}$, $\tilde{v}$, or $\tilde{b}$; $\tilde{g}_a$ and ϕ_g are the amplitude and the phase of g; $\tilde{g}_r$ and $\tilde{g}_i$ are real and imaginary parts of g.

b. *Energetics of unstable modes*

Equations for alongfront averaged perturbation kinetic and potential energy can be obtained from (2.1):

$$\frac{\partial}{\partial t}\left(\frac{\overline{u^2 + v^2}}{2h}\right) = -\left(\frac{\partial \overline{u\pi}}{\partial x} + \frac{\partial \overline{v\pi}}{\partial y} + \frac{\partial \overline{\omega\pi}}{\partial \zeta}\right) - \mathrm{Ro}\left(\frac{V_x}{h}\overline{uv} + \frac{V_\zeta}{h}\overline{v\omega}\right) + (\zeta - 1)\frac{1}{h}\frac{\partial h}{\partial x}\overline{ub} + \overline{\omega b} \quad \text{(C.6a)}$$

$$\frac{\partial}{\partial t}\left(\frac{\overline{b^2}}{2SB_\zeta}\right) = -\frac{B_x}{B_\zeta}\overline{ub} - \overline{\omega b}. \quad \text{(C.6b)}$$

The term on the right-hand side of (C.6a) and (C.6b) are possible sources and sinks of perturbation energies. The first term on the right-hand side of (C.6a) represents pressure work; it does not contribute to the cross-sectional averaged kinetic energy. The Reynolds stress term, the conversion of the mean kinetic energy to eddy kinetic energy, is defined as

$$\mathrm{RS} = -\mathrm{Ro}\left(\frac{V_x}{h}\overline{uv} + \frac{V_\zeta}{h}\overline{v\omega}\right). \quad \text{(C.7)}$$

The vertical and horizontal heat flux correlations represent the conversion of the eddy potential energy to the eddy kinetic energy and the conversion of the mean potential energy to the eddy potential energy, respectively:

TABLE D.1. Comparison of wave frequency in a flat bottom channel between the analytic and numerical solutions. This calculation is based on $\beta = 6.0$, $L = 4.0$ and $S = 1.0$.

	v/λ					
	1/0	1/2	2/0	2/2	3/0	3/2
Analytic	1.9099	2.2130	0.9549	1.4051	0.6366	1.1971
$M = N = 10$	1.9099	2.2128	0.9549	1.4034	0.6366	1.1936
$M = N = 15$	1.9099	2.2130	0.9549	1.4050	0.6366	1.1968
$M = N = 20$	1.9099	2.2130	0.9549	1.4051	0.6366	1.1970

$$\text{VHF} = \overline{\omega b} + (\zeta - 1)\frac{1}{h}\frac{\partial h}{\partial x}\overline{ub} \qquad \text{(C.8)}$$

$$\text{HHF} = \left((\zeta - 1)\frac{\partial h}{\partial x} - \frac{B_x}{B_z}\right)\frac{1}{h}\overline{ub}. \qquad \text{(C.9)}$$

A mean state is said to be baroclinically unstable in the case that waves grow due to positive horizontal and vertical heat fluxes, whereas it is said to be barotropically unstable in the case that waves grow due to positive Reynolds stresses. Frontal zones under consideration have nontrivial variations in both horizontal and vertical directions, and as a result, both mechanisms will in general be operational.

APPENDIX D

Verification of the Model

a. Stable wave solutions in a flat bottom channel

We consider a flat bottom channel and assume no mean flow and uniform stratification. Analytical solutions are provided for comparison. The barotropic solution is characterized by $\sigma = \pm 1$; corresponding eigen functions are indeterminable. However, there are two sets of baroclinic solutions. The first is the coastal trapped Kelvin waves, characterized by $u = 0$. Their frequencies are $\sigma_r = \pm\sqrt{S\beta\nu\pi}$ and $\sigma_i = 0$, $\nu = 1, 2, \cdots$. The second solution is the Poincaré waves that span across the channel:

$$\sigma_r^2 = 1 + \frac{S}{\nu^2}\left[\left(\frac{\beta}{\pi}\right)^2 + \left(\frac{\lambda}{L}\right)^2\right] \quad \text{and} \quad \sigma_i = 0$$
$$(\lambda > 0, \nu = 1, 2, \cdots). \qquad \text{(D.1)}$$

In all numerical calculations σ_i is zero for every mode; $\lambda = 0$ corresponds to coastal trapped Kelvin waves, and their frequencies are calculated with a very high accuracy even for a low truncation level. Frequencies of Poincaré waves are calculated with small errors, but these errors decrease as the truncation level increases, as shown in Table D.1. Overall, the error is the order of 10^{-4} for the first few modes. Generally speaking, the model is very successful in capturing mode structures.

b. Cross-channel topographic gradient

We again consider a channel with no mean flow, but a topographic gradient is included so that $B_x = (\zeta - 1)(dh/dx)N^2$ and $B_\zeta = N^2 h(x)$. Such a system should be stable because there are no energy sources. However, numerical results generally show a few modes with rather small growth rates. Numerical calculations are based on $h(x) = h_1 - h_2 \cos(\pi x/L)$, $N^2 = 1$, so that the derivatives and integrals can be easily calculated analytically without introducing errors. Two possible sources of error in the calculation are 1) the truncation error and 2) ϵ_b, the error induced by the inconsistency of the lower boundary condition. Although the collocation scheme used in the buoyancy equation avoids obvious violation of the boundary condition (2.8b) and the Gibbs phenomenon inside the domain, it does not resolve the gap between the boundary and the first collocation point; ϵ_b depends upon the value of B_x at the bottom; thereby, it depends upon the bottom slope and the stratification. Moreover, it may increase as the truncation level increases because the first collocation point becomes closer to the lower boundary where the boundary condition is not completely satisfied. Experiments with various topographies and stratifications have been accomplished to determine the range of ϵ_b. Generally speaking, ϵ_b increases as the bottom slope increases. However, the relationships between ϵ_b and stratification or truncation are not so obvious. What is important is that in all experiments ϵ_b is less than 10^{-3}! Therefore, the error induced by the inconsistency of the lower boundary constraint will not significantly affect the discussion of the Gulf Stream stability since the growth rates is at least one or two orders larger.

REFERENCES

Bane, J. M. Jr., 1983: Initial observations of the subsurface structure and short-term variability of the seaward deflection of the Gulf Stream off Charleston, South Carolina. *J. Geophys. Res.*, **88**, 4673–4684.

——, and W. K. Dewar, 1988: Gulf Stream bimodality and variability downstream of the Charleston Bump. *J. Geophys. Res.*, **93**, 6695–6710.

——, D. A. Brooks, and K. R. Lorenson, 1981: Synoptic observations of the three-dimensional structure and propagation of the Gulf Stream meanders along the Carolina continental margin. *J. Geophys. Res.* **86**, 6411–6425.

Blumsack, S. L., and P. J. Gierasch, 1972: Mars: The effects of topography on baroclinic instability. *J. Atmos. Sci.*, **29,** 1081–1089.

Boyd, J. P., 1982: The optimization of convergence for Chebyshev polynomial methods in unbounded domain. *J. Comput. Phys.*, **45,** 43–79.

Brooks, D. A., and J. M. Bane, Jr., 1981: Gulf Stream fluctuations and meanders over the Onslow Bay upper continental slope. *J. Phys. Oceanogr.*, **11,** 247–256.

——, and ——, 1983: Gulf Stream meanders off North Carolina during winter and summer 1979. *J. Geophys. Res.*, **88,** 4633–4650.

Charney, J. G., 1947: The dynamics of long waves in a baroclinic westerly current. *J. Meteor.*, **4,** 135–163.

Dewar, W. K., and J. M. Bane Jr., 1985: Subsurface energetics of the Gulf Stream near the Charleston Bump. *J. Phys. Oceanogr.*, **15,** 1771–1789.

De Szoeke, R. A., 1975: Some effects of bottom topography on baroclinic instability. *J. Mar. Res.*, **33,** 93–122.

Eady, E. T., 1949: Long waves and cyclone waves. *Tellus*, **1,** 33–52.

Gaster, M., 1962: A note on a relation between temporally increasing and spatially increasing disturbances in hydrodynamic instability. *J. Fluid Mech.*, **14,** 222–224.

Hogg, N. G., 1976: On spatially growing baroclinic waves in the ocean. *J. Fluid Mech.*, **78,** 217–235.

Hood, C. A., and J. M. Bane Jr., 1983: Subsurface energetics of the Gulf Stream cyclonic frontal zone off Onslow Bay, North Carolina. *J. Geophys. Res.*, **88,** 4651–4662.

Johns, W. E., 1988: One-dimensional baroclinically unstable waves on the Gulf Stream potential vorticity gradient near Cape Hatteras. *Dyn. Atmos. Oceans*, **11,** 323–350.

Leaman, K. D., E. Johns, and T. Rossby, 1989: The averaged distribution of volume transport and potential vorticity with temperature at three sections across the Gulf Stream. *J. Phys. Oceanogr.*, **19,** 36–51.

Lee, T. N., and D. A. Mayer, 1977: Low-frequency current variability and spin-off eddies along the shelf off Southeast Florida. *J. Mar. Res.*, **35,** 193–220.

——, and L. P. Atkinson, 1983: Low-frequency current and temperature variability from Gulf Stream frontal eddies and atmospheric forcing along the Southeast U.S. outer continental shelf. *J. Geophys. Res.*, **88,** 4541–4567.

——, and E. Waddell, 1983: On Gulf Stream variability and meanders over the Blake Plateau at 30°N. *J. Geophys. Res.*, **88,** 4617–4631.

——, L. P. Atkinson, and R. Legeckis, 1981: Observations of a Gulf Stream frontal eddy on the Georgia continental shelf, April 1977. *Deep-Sea Res.*, **28A,** 347–378.

Legeckis, R. V., 1979: Satellite observations of the influence of bottom topography on the seaward deflection of the Gulf Stream off Charleston, South Carolina. *J. Phys. Oceanogr.*, **9,** 483–497.

Luther, M. E., and J. M. Bane, Jr., 1985: Mixed instabilities in the Gulf Stream over the continental slope. *J. Phys. Oceanogr.*, **15,** 3–23.

McIntyre, M. E., 1970: On the non-separable baroclinic parallel flow instability problem. *J. Fluid Mech.*, **40,** 273–306.

Mellor, G. L., 1962: A general solution to the laminar flow in wakes. *J. Appl. Mech.*, 589–590.

Moore, G. W. K., and W. R. Peltier, 1987: Cyclogenesis in frontal zones. *J. Atmos. Sci.*, **44,** 384–409.

——, and ——, 1989a: Non-separable baroclinic instability. Part I: Quasi-geostrophic dynamics. *J. Atmos. Sci.*, **46,** 57–78.

——, and ——, 1989b: Frontal cyclogenesis and the geostrophic momentum approximation. *Geophys. Astrophys. Fluid Dyn.*, **45,** 183–197.

——, and ——, 1990: Non-separable baroclinic instability. Part II: primitive equation dynamics. *J. Atmos. Sci.*, **47,** 1223–1242.

Nakamura, N., 1988: Scale selection of baroclinic instability—Effects of stratification and nongeostrophy. *J. Atmos. Sci.*, **45,** 3253–3267.

Oey, L-Y, 1988: A model of Gulf Stream frontal instabilities, meanders and eddies along the continental slope. *J. Phys. Oceanogr.*, **18,** 211–228.

Orlanski, I., 1969: The influence of bottom topography on the stability of jets in a baroclinic fluid. *J. Atmos. Sci.*, **26,** 1216–1232.

Richardson, W. S., W. J. Schmitz, Jr., and P. P. Niiler, 1969: The velocity structure of the Florida Current from the straits of Florida to Cape Fear. *Deep-Sea Res.*, **16,** 447–470.

Stern, M. E., 1985: Lateral wave breaking and "shingle" formation in large-scale shear flow. *J. Phys. Oceanogr.*, **15,** 1274–1283.

Stone, P. H., 1966: On non-geostrophic baroclinic stability. *J. Atmos. Sci.*, **23,** 390–400.

——, 1970: On non-geostrophic baroclinic stability: Part II. *J. Atmos. Sci.*, **27,** 721–726.

Webster, F., 1961: A description of Gulf Stream meanders off Onslow Bay. *Deep-Sea Res.*, **8,** 130–143.